Numerical simulations of plastic deformation and fracture effects in two phase γ-TiAl + α_2-Ti$_3$Al lamellar microstructures

By BIMAL K. KAD, MING DAO and ROBERT J. ASARO

Department of Applied Mechanics and Engineering Sciences,
University of California-San Diego, La Jolla, CA 92093-0411, USA

ABSTRACT

Deformation characteristics of fully lamellar (FL) and nearly lamellar (NL) morphologies in two phase γ-TiAl(L1$_0$) + α_2-Ti$_3$Al(D0$_{19}$) polycrystalline aggregates are simulated by finite element methods. Polycrystalline stress–strain response is accurately predicted using, as input parameters, the range of soft (τ_{crss}^{soft}) and hard (τ_{crss}^{hard}) mode critical resolved shear stresses obtained from single poly-synthetically twinned lamellar crystals, for shear parallel and perpendicular to the lamella. The deformation is severely inhomogeneous, due in part to the large difference in τ_{crss}^{soft} and τ_{crss}^{hard}, with the largest strain accumulations being encountered at grain boundaries, particularly at triple points. Such deformation incompatibilities between adjacent crystals create large hydrostatic stress concentrations at grain boundaries, which are likely nucleation sites for fracture, as experimentally verified for both tension and compression loading. Incorporating small volume fractions of γ-TiAl (with compliant deformation characteristics, at least at small strains) at grain boundaries, as in the case for NL microstructures, greatly reduces the magnitude of the peak hydrostatic stresses, and consequently mitigates fracture initiation. This provides a suitable explanation for the increase in ductility as associated with an increasing volume fraction of γ-TiAl in lamellar microstructures. It is shown that numerically computed plots of hydrostatic stress against strain provide a more logical *and* direct correlation between microstructure and ductility response, over the current, more traditional stress–strain plots.

§1. INTRODUCTION

Two-phase γ-TiAl(L1$_0$) + α_2-Ti$_3$Al(D0$_{19}$) alloys with fine scale (approximately 1–2 μm) lamellar microstructures exhibit improved ductility and fracture toughness over their monolithic constituents. Consequently there has been much interest in developing these two-phase alloys as viable materials for high-temperature structural applications. The room temperature (RT) mechanical behaviour of single poly-synthetically twinned (PST) lamellar crystals has been reported in tension (Inui, Oh, Nakamura and Yamaguchi 1992), compression (Fujiwara *et al.* 1990), and for varying lamella thicknesses (Umakoshi, Nakano and Yamane 1991, Nakano, Yokoyama and Umakoshi 1992). A comprehensive review of the recent developments is given by Yamaguchi and Umakoshi (1990). These beneficial improvements have been realized largely in single crystals (or colonies) of lamellar material, and it has been impossible to transpose the single crystal behaviour to polycrystalline aggregates which typically fail at tensile strains less than 3%. While single crystal properties are attractive, their application is certainly cost prohibitive. Thus, a means to identify and incorporate appropriate improvements in conventionally processed polycrystalline microstructures remains an important, though formidable, engineering challenge.

    In this paper, we attempt to explore (i) the micromechanics of deformation in two-phase γ-TiAl + α_2-Ti$_3$Al polycrystalline alloys, (ii) the constraint based strengthening in two-phase polycrystalline aggregates as derived from neighbouring grains, and (iii) the implications of microstructural variations on the flow and fracture behaviour of the two phase γ-TiAl + α_2-Ti$_3$Al alloys. In particular, the effects of lamellar morphology in controlling crystal plasticity are explored. We use numerical techniques to simulate the deformation characteristics of polycrystalline aggegates. The exercise involves using single crystal property data to describe the constitutive response on the micro-scale to predict macroscopic flow behaviour.

    The plan of the paper is as follows: the specific details of single and polycrystal mechanical behaviour are described briefly in § 1. The theoretical concepts and the numerical methodology is outlined in § 2. The γ-TiAl + α_2-Ti$_3$Al alloy specific details and adaptation of the mechanical properties as employed in the two-dimensional plane strain finite element calculations are outlined in § 3. The experimental and computational results are presented and specific features of the deformation process are discussed in § 4. § 5 discusses salient features of this work along with our summary and conclusions.

1.1. *General background*

    Ti–(48–50) at.%Al alloys, of engineering interest, initially solidify as disordered α-hexagonal-close packed (h.c.p.) (fig. 1) which upon cooling undergo the solid state transformations $\alpha \rightarrow \gamma$ and $\alpha_2 \rightarrow \gamma$ yielding the laminate morphology. The lamellar geometry is comprised of flat slabs of α_2-Ti$_3$Al and γ-TiAl with an h.c.p.-face-centred cubic (f.c.c.) type orientation relationship as $(0001)\alpha_2 \| \{111\}\gamma$ and $\langle 11\bar{2}0 \rangle \alpha_2 \| \langle 1\bar{1}0 \rangle \gamma$

Fig. 1
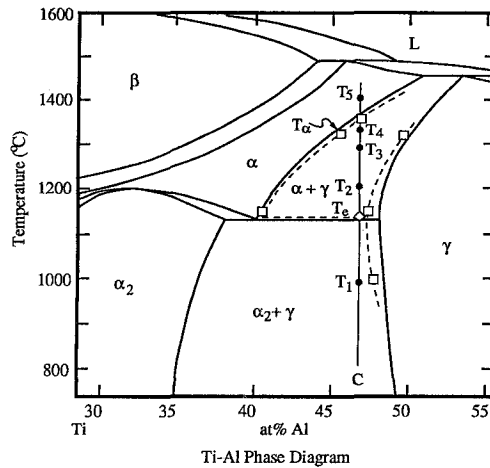
Ti–Al Phase Diagram

Ti–Al phase diagram of interest for thermomechanical processing of Ti–(48–50) at.%Al two phase alloys. A variety of microstructures can be obtained by thermomechanical treatments depending on such conditions as heat treatment temperature and time, cooling rate and scheme. Common heat-treatment regimes are indicated on the phase diagram as T_α, $T_{\text{near}\,\alpha\,\text{transus}}$, $T_{\alpha+\gamma}$ yielding fully lamellar (FL), nearly lamellar (NL) and duplex (D) microstructures, respectively (reproduced from Kim (1989)).

in a given colony. The unique orientation of the basal plane normal in the parent α-h.c.p. phase, thus determines the eventual orientation of the flat slabs in the polycrystalline aggregate.

A variety of polycrystalline microstructures (consequently with varying mechanical behaviour) can be obtained by post-solidification thermal treatments (see fig. 1) depending on such conditions as heat treatment temperature and time, cooling rate and scheme (Kim 1992), and ageing temperature and time. The microstructures have been previously divided into four groups: near-gamma (NG), duplex (D), nearly lamellar (NL), and fully lamellar (FL) microstructures. For Ti–(48–50) at.%Al alloys, the thermo-mechanical treatments of interest, yielding the best combinations of mechanical properties, are in the vicinity of the $\alpha/\alpha + \gamma$ phase boundary. For samples in the α phase field, the expected microstructure upon continuous cooling is fully lamellar and its scale is determined by holding time at temperature (accounting for grain size) and the cooling rate (accounting for lamellar widths). For specimens in the $\alpha + \gamma$ phase field, the duplex microstructure is controlled by holding temperature (accounting for the equilibrium volume fractions of the constituent phases), holding time (accounting for approaching equilibrium volume fractions) and cooling rate (which as before determines the lamellar thickness).

1.1.1. *Single crystal response*

In the laminate form, γ-TiAl is the softer phase and a flow anisotropy is derived particularly from the laminate geometry such that shear deformation parallel to the slabs (soft mode τ_{crss}^{soft}) is easier than across the slabs (hard mode τ_{crss}^{hard}) where γ slip encounters the harder α_2-phase (Fujiwara *et al.* 1990). The deformation path length ratio for soft and hard mode is about 100. The Hall–Petch slopes are in themselves anisotropic, with $k = 0.273$ and $0.440 \, \text{MPa}/\sqrt{m}$ for soft and hard modes, respectively (Nakano *et al.* 1992). The nature of specific crystallographic interface barriers and their contribution to yield stress, for specific perfect or superdislocation, soft and hard mode slip systems is discussed by Kad, Hazzledine and Fraser (1993).

The single crystal mechanical response is severely anisotropic, as manifested by its various macroscopic, microscopic and crystal structure anisotropies.

1.1.1.1. *Macroscopic anisotropy.*

The mechanical behaviour anisotropies pertain to (i) flow stress, (ii) fracture stress, (iii) fracture strain, and (iv) crack growth rate. The strength of lamellar single crystals is orientation dependent, fig. 2. In an analogous manner, single colonies also exhibit orientation dependent fracture strains and, except for the case of the hard mode, exhibit a superior ductile behaviour (i.e., they display tensile fracture strains up to about 30%, Inui *et al.* 1992), see fig. 2. In addition, fatigue crack growth exhibits a rate anisotropy of 2.7×10^{-7} m/cycle against 7×10^{-7} m/cycle respectively for growth perpendicular and parallel to the laminates (Davidson and Campbell 1993).

1.1.1.2. *Microscopic anisotropy.*

The microscopic effects largely pertain to (i) large differences between the critical resolved shear stresses (i.e. τ_{crss}^{soft} and τ_{crss}^{hard}) of the slip systems belonging to the respective constituents as well as within a given constituent, (ii) the contribution of a particular slip system to the overall deformation, under specific conditions of temperature and strain rate, and (iii) alloying and more importantly, impurity considerations, in that whether they aid or exacerbate critical resolved shear stress (CRSS) differences of specific slip systems. Specific details of the

Fig. 2
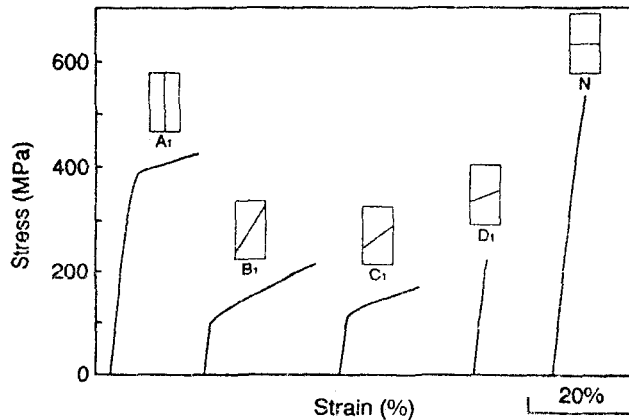
Orientation dependent stress strain behaviour in single crystals of lamellar TiAl (reproduced from Inui *et al.* (1992)).

microscopic and macroscopic anisotropies of single lamellar (PST) crystals are described in §3 along with their incorporation into the numerical model.

1.1.2. *Polycrystal response*

The unique orientation of the basal plane normal in the parent α-h.c.p. phase determines the eventual orientation of the flat slabs in the polycrystalline aggregate. As a result, the orientation dependence of single crystals, described above, are implicitly present in the random polycrystalline aggregates. In addition, further variations in mechanical behaviour are observed, based on the shape, phase and volume effects of the constituent mix, see fig. 3. The microstructural dependence of tensile elongation and fracture toughness is significantly dramatic, and the ductility and fracture toughness parameters exhibit an 'inverse-ductility–toughness' relationship (Kim 1992) for the lamellar and duplex alloys. Thus fully lamellar alloys have low ductilities and high fracture toughness ($K_{1C} \approx 22$–$32 \, MPa \sqrt{m}$), whereas nearly lamellar and duplex alloys have high ductilities and low fracture toughness ($K_{1C} \approx 10$–$12 \, MPa \sqrt{m}$) (Kim 1992). This increased toughness in FL microstructures has recently been attributed to features such as crack deviation, crack bridging, and crack surface tortuosity (Chan and Kim 1991, 1992).

1.2. *Statement of the problem*

Whilst modest improvements in tensile ductility (i.e. fracture strains on the order of 30%) have been realized in single crystals (or a single colony) of lamellar material (Inui *et al.* 1992), polycrystalline aggregates, in comparison, perform poorly in tension (Kim 1992). Consequently, there exists a large disparity in mechanical behaviour between single and polycrystals. It appears that this severe downturn in mechanical response arises from some form of grain boundary constraints (an additional variable) in polycrystalline aggregates. One peculiar aspect of this problem is that both the polycrystalline yield stress, and strain to failure, almost always approach the single crystal hard mode behaviour.

While disparities in polycrystalline mechanical behaviour have been exhaustively reported, the microstructural subtleties responsible for such variations are not understood. An additional complexity is that apart from the grain size dependence of yield strength, most microstructural variations have little influence on the flow curve, or the work hardening behaviour (Kim 1992) as they all fall in a relatively narrow band (see fig. 3) with similar work hardening characteristics. Thus, monitoring the flow curve in itself may *not* be an optimum control parameter, as quasi-static test performance (i.e., ductility) may be decidedly different from fracture toughness (i.e.,

Fig. 3
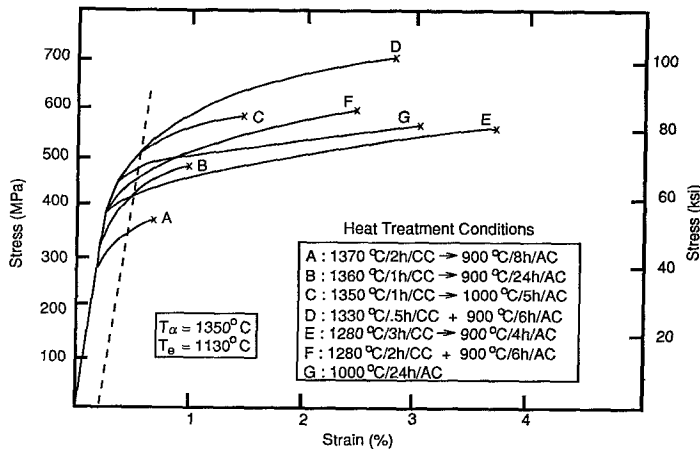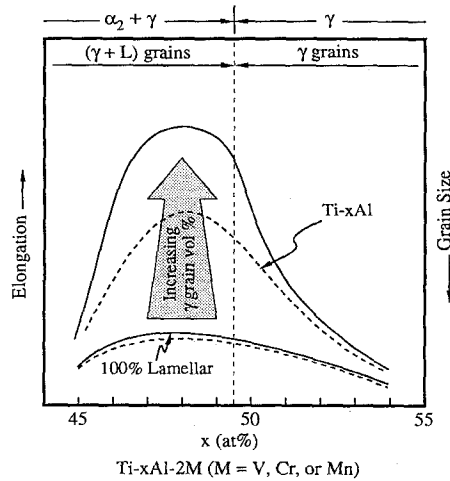
(*a*) Stress–strain flow curves for the fully lamellar (FL), nearly lamellar (NL) and duplex (D) microstructures as tested at ambient temperatures (reproduced from Kim (1992)). (*b*) Schematic of the microstructural effects of increasing γ volume fraction on tensile elongation in (FL), (NL) microstructures (reproduced from Kim (1989)).

K_{1C}) as is manifested by the 'inverse-ductility–toughness' relationship (Kim 1992). For example, the flow stress behaviour of the FL and NL materials are roughly similar, but this offers no clues as to why the ductilities and the fracture toughness are different. It is apparent that relatively small variations in thermo-mechanical treatments (thereby yielding a slightly different microstructural mix) radically effect ductile response, as seen in fig. 3. However, from a mechanistic perspective, it is not immediately obvious what these subtle changes entail. In particular, the functional dependence of an improvement in ductility on increasing volume fraction of γ-TiAl, remains unexplained to date. The problem is further complicated for TiAl based ternary alloys, where observed improvements in mechanical behaviour may very well be due to minor changes in the morphology, or microstructural mix, arising out of slight shifts in the phase boundaries (fig. 1).

1.3. Objectives and concepts

The objective of this work is to provide a suitable rationale for the experimentally observed disparities between single and polycrystalline materials, and to understand the subtleties of microstructural effects. An important prerequisite of a suitable design approach is the ability to predict the essential and characteristic contribution of the individual micro-constituents (i.e., lamellar grains or γ-grains) in the polycrystalline deformation behaviour. Towards this end, numerical techniques, originally derived from the Taylor model (Taylor 1938 a), but extended to include elastic-viscoplastic behaviour *and* low symmetry crystals, are employed to compute and predict the global response of polycrystals. Thus, it is possible to use the single crystal mechanical property data as input to predict the aggregate polycrystalline behaviour. Such a computational technique is routinely employed to predict the development of deformation textures and the constitutive behaviour of polycrystals subjected to large strains (Taylor 1938 a, Bishop 1954, Dillamore and Katoh 1974). One specific shortfall of the Taylor model, i.e., the assumption that each grain in the polycrystal is subject to the same uniform strain as the aggregate, is of particular interest in the present context. The premise for such an argument is that specific inhomogeneities may occur in the deforming crystal (Dillamore and Katoh 1974, Harren and Asaro 1989). Harren and Asaro (1989) employed finite element techniques for ductile f.c.c. or body-centred cubic (b.c.c.) polycrystals, to rigorously account for these effects and revealed that non-uniform deformations, and strain localizations naturally arise in polycrystals as a consequence of the crystallographic slip process. Further, these finite element calculations provide physical insight into identifying the mechanisms that contribute to localized deformation effects. Since localized regions are prevalent in large strain deformations, they must affect, to some degree, the global stress–strain response and mechanical behaviour in general. For example, lamellar TiAl exhibits a large plastic flow anisotropy for shear deformation parallel to (soft mode deformation), and across (hard mode deformation) the lamellar boundaries. On account of this large (orientation dependent) flow stress anisotropy, it is plausible that non-uniform deformations occur in randomly stacked polycrystalline aggregates. It appears somewhat counterintuitive, that non-uniform effects may contribute a decisive role, especially at low strains (2 to 3%). However, we note that the non-uniform effects were originally computed for ductile aluminium and copper with 12 identical slip systems (and five independent slips systems satisfying the Von Mises criteria of macroscopic plasticity), where localizations nominally require higher strains. Similarly, incompatibilities arising out of specific misorientations between

adjacent crystals are also muted on account of the 12 slip systems available. These effects are expected to be exacerbated in the event of (i) limited availability of slip systems, and (ii) a large difference in CRSS for the individual slip systems. Both problems (i) and (ii) exist in two phase γ-TiAl+α_2-Ti$_3$Al lamellar microstructures and strain incompatibilities (and consequently, the development of large stresses) across neighbouring crystals are a natural outcome of such limitations. For the case of lamellar TiAl, an understanding of such localized behaviour is important since they might be precursors to material failure. Thus studying such localization effects may play an important role in addressing mechanical response. This current work provides clues and symptoms pertaining to material failure, with respect to single crystal behaviour and microstructural variations.

§2. THEORY AND NUMERICAL CONSIDERATIONS

Standard tensor notation is used throughout the following development. Bold faced symbols are used to denote vectors and higher-order tensors, the order of which will be clear in context. Products are indicated with dots, which denote summation over repeated Latin indices, and products containing no dots are dyadic products. Latin indices ranged from one to the number of spatial dimensions, and repeated Latin indices are always summed. Inverses, transposes, and transposed inverses are denoted with a superscripted -1, T and $-$T, respectively and superposed dots indicate differentiation with respect to time t. For example,

$$\mathbf{A} \cdot \mathbf{B} = A_{ik}B_{kj}\mathbf{b}_i\mathbf{b}_j; \qquad \mathbf{A} \times \mathbf{B} = e_{ijk}A_jB_k\mathbf{b}_i;$$

$$\mathbf{A} : \mathbf{B} = A_{ij}B_{ji}; \qquad \mathbf{AB} = A_{ij}B_{kl}\mathbf{b}_i\mathbf{b}_j\mathbf{b}_k\mathbf{b}_l;$$

$$\mathbf{cd} = c_id_j\mathbf{b}_i\mathbf{b}_j; \qquad \mathbf{B} \cdot \mathbf{c} = B_{ij}c_j\mathbf{b}_i;$$

$$\frac{\partial \mathbf{c}}{\partial \mathbf{d}} = \frac{\partial c_i}{\partial d_j}\mathbf{b}_i\mathbf{b}_j; \qquad \dot{\mathbf{B}} = \frac{\partial B_{ij}}{\partial t}\mathbf{b}_i\mathbf{b}_j;$$

$$\mathbf{H} : \mathbf{A} = H_{ijkl}A_{lk}\mathbf{b}_i\mathbf{b}_j,$$

where e_{ijk} is the permutation symbol. The basis, $\mathbf{b}_i$, is Cartesian and independent of time. Greek indices are used to identify slip systems and range from one to N = the number of slip systems. Summation over repeated nonparenthetical Greek indices is implied while repeated parenthetical Greek indices are not summed, e.g., $\mathbf{c}_\alpha\mathbf{d}_\alpha$ means $\mathbf{c}_1\mathbf{d}_1 + \mathbf{c}_2\mathbf{d}_2 + \cdots + \mathbf{c}_N\mathbf{d}_N$ and $\mathbf{c}_\alpha\mathbf{d}_{(\alpha)}$ means either $\mathbf{c}_1\mathbf{d}_1$, $\mathbf{c}_2\mathbf{d}_2$, ..., or $\mathbf{c}_N\mathbf{d}_N$.

2.1. *Single crystal constitutive law*

The constitutive theory that is used in the analyses presented here is a rate dependent thermoelastic-viscoplastic, finite strain, crystallographic slip theory incorporating non-Schmid effects. The theory, in its present form, was developed by Asaro and his coworkers (Asaro (1979), Pierce, Asaro and Needleman (1982, 1983), Harren, Dève and Asaro (1988), McHugh, Asaro and Shih (1993) and, most recently Dao and Asaro (1993)). The theory builds on the pioneering work of Taylor (1938 b) and the more recent work of Hill and Rice (1972).

The reference configuration is taken to be a defect-free perfect crystal, with an undeformed, stress free lattice along with its embedded material. The position of each material particle is given in this reference configuration by its position vector $\mathbf{X}$. In this reference configuration, slip systems, designated and numbered by Greek letters

Fig. 4
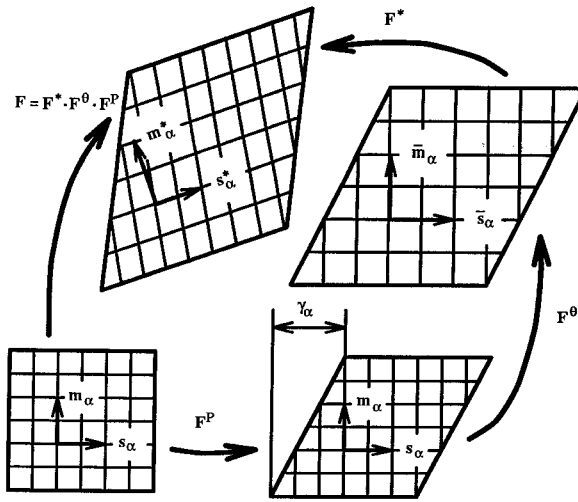
Schematic of the decomposition of the deformation gradient **F** into plastic shear part **F**^{P}, thermal deformation part **F**$^\theta$, and elastic plus lattice rotational part **F***. In the current study **F**$^\theta$ = **I** for isothermal deformation simulations, where **I** is the second-order identity tensor.

are defined by the orthogonal pair of unit vectors ($\mathbf{s}_\alpha$, $\mathbf{m}_\alpha$), where $\mathbf{s}_\alpha$ is parallel to the α slip direction in the recent configuration and $\mathbf{m}_\alpha$ is normal to its slip plane. Note that such vectors are embedded in the crystal's lattice and will convect with it, i.e. they deform and rotate with the lattice in ways defined by models for plastic flow. The current configuration is defined as the elastically, thermally, and plastically deformed crystal, where the current position of each material particle is described by its current position vector **x**. The displacement vector, **u**, is given by **u** = **x** − **X**, and the deformation gradient **F** that maps the current configuration from the reference is given by **F** = $\partial\mathbf{x}/\partial\mathbf{X}$ = **I** + $\partial\mathbf{u}/\partial\mathbf{X}$, where **I** is the second-order identity tensor. In order to reach the current configuration from the reference, the plastic, thermal, and elastic parts of the total deformation are decomposed according to the kinematic scheme illustrated in fig. 4.

One imagines that the material flows through the undeformed lattice by shear along the various slip systems of the crystal to reach the first intermediate configuration. The spatial velocity gradients of this plastic shear flow are written as

$$\dot{\mathbf{F}}^P \cdot \mathbf{F}^{P-1} = \dot{\gamma}_\alpha s_\alpha \mathbf{m}_{(\alpha)}, \tag{1}$$

where $\dot{\gamma}_\alpha$ is the shear rate on the αth slip system and **F**^{P} is the plastic part of the deformation gradient. The value of **F**^{P} is given by the path dependent integration of (1).

From this plastically sheared state the second intermediate configuration is reached by imagining the crystal undergoing a general thermal deformation described by the thermal part of the deformation gradient, **F**$^\theta$, where θ represents temperature. The spatial velocity gradients corresponding to this thermal deformation are written as

$$\dot{\mathbf{F}}^{\theta} \cdot \mathbf{F}^{\theta-1} = \dot{\theta}\boldsymbol{\alpha}, \qquad \boldsymbol{\alpha} = \alpha_{ij}\mathbf{a}_i\mathbf{a}_j, \tag{2}$$

where $\boldsymbol{\alpha}$ is a tensor whose components, α_{ij}, with respect to the time independent Cartesian base vectors, $\mathbf{a}_i$, are the thermal expansion coefficients. The base vectors are aligned with the crystal lattice in the reference configuration in some standard way, e.g., in cubic crystals, it is most convenient to align the $\mathbf{a}_i$ base vectors with the cube axes, in which case $\boldsymbol{\alpha}$ would be diagonal with all components equal.

The current configuration is reached by elastic deformation, along with possible rigid body rotation of the crystal lattice along with its embedded material. This part of the deformation is described by $\mathbf{F}^*$, the lattice part of the deformation gradient. Hence according to the scheme described in fig. 4, one obtains the deformation gradient decomposition,

$$\mathbf{F} = \mathbf{F}^* \cdot \mathbf{F}^{\theta} \cdot \mathbf{F}^{\mathrm{P}}. \tag{3}$$

Here, $\mathbf{F}$ is the deformation gradient describing the complete deformation. In reality the elastic distortion of the lattice, thermal deformation and plastic flow occur simultaneously, but it is clear that the current configuration of this model crystal can be reached by the above imagined steps of deformation. For concise further presentation of this development, we combine the various parts of the deformation gradient as follows,

$$\hat{\mathbf{F}} = \mathbf{F}^{\theta} \cdot \mathbf{F}^{\mathrm{P}}, \quad \text{and} \quad \bar{\mathbf{F}} = \mathbf{F}^* \cdot \mathbf{F}^{\theta}. \tag{4}$$

The *loading parameter* to load slip system α, $\tau_{\alpha}^{\mathrm{D}}$ (Asaro and Rice 1977, Dao and Asaro 1993), is given as

$$\tau_{\alpha}^{\mathrm{D}} = \tau_{\alpha} + \boldsymbol{\eta}_{\alpha} : \boldsymbol{\tau} = \mathbf{m}_{\alpha}^* \cdot \boldsymbol{\tau} \cdot \mathbf{s}_{\alpha}^* + \boldsymbol{\eta}_{\alpha} : \boldsymbol{\tau}, \tag{5a}$$

$$\mathbf{s}_{\alpha}^* = \bar{\mathbf{F}} \cdot \mathbf{s}_{\alpha}; \qquad \mathbf{m}_{\alpha}^* = \mathbf{m}_{\alpha} \cdot \bar{\mathbf{F}}^{-1}; \qquad \mathbf{z}_{\alpha}^* = \mathbf{s}_{\alpha}^* \times \mathbf{m}_{\alpha}^*, \tag{5b}$$

$$\boldsymbol{\tau} = J\boldsymbol{\sigma}, \tag{5c}$$

where $J = \det\{\mathbf{F}\}$ is the Jacobian, $\boldsymbol{\tau}$ is the Kirchhoff stress tensor, $\boldsymbol{\sigma}$ is the Cauchy stress tensor, $\mathbf{s}_{\alpha}^*$ is along the αth slip direction in the current configuration, $\mathbf{m}_{\alpha}^*$ is normal to the αth slip plane, $\mathbf{z}_{\alpha}^*$ is normal to both $\mathbf{s}_{\alpha}^*$ and $\mathbf{m}_{\alpha}^*$, and $\boldsymbol{\eta}_{\alpha}$ is the tensor of non-Schmid effects for slip system α which, when aligned with $\mathbf{s}_{\alpha}$, $\mathbf{m}_{\alpha}$ and $\mathbf{z}_{\alpha}$, takes the simple form,

$$\boldsymbol{\eta} = \begin{bmatrix} \eta_{ss} & 0 & \eta_{sz} \\ 0 & \eta_{mm} & \eta_{mz} \\ \eta_{sz} & \eta_{mz} & \eta_{zz} \end{bmatrix}. \tag{6}$$

The kinetic description of plasticity on each slip system is cast in terms of the *loading parameter* $\tau_{\alpha}^{\mathrm{D}}$ and the slip rate on that system as

$$\dot{\gamma}_{\alpha} = \dot{a}\,\mathrm{sgn}\,(\tau_{\alpha})\left(\left|\frac{\tau_{(\alpha)}^{\mathrm{D}}}{g_{(\alpha)}}\right|\right)^{\frac{1}{m}}, \tag{7}$$

where τ_{α} is the current value of the resolved shear stress, $\tau_{\alpha}^{\mathrm{D}}$ is the *loading parameter* for slip as defined in (5), and $g_{\alpha} > 0$ is the current value of the *slip system hardness*. In (7), m is the material rate sensitivity exponent (which will, in the examples described herein, be taken the same for each slip system), and $\dot{a}$ is the reference shear rate. The

slip system hardness g_α is obtained by the path dependent integration of the evolution equation

$$\dot{g}_\alpha = h_{\alpha\beta}(\gamma_a)|\dot{\gamma}_\beta| + g_\alpha^\theta \dot{\theta}, \qquad \gamma_a = \int_0^t \sum_\alpha |\dot{\gamma}_\alpha|\, \mathrm{d}t, \qquad (8)$$

where $h_{\alpha\beta}$ is a matrix of (positive) hardening moduli, g_α^θ is the rate of change of slip system hardness with respect to temperature alone, and γ_a is the accumulated sum of slips. The initial condition for this evolution are given by $g_\alpha(\gamma_a = 0, \ \theta = \theta_0) = g_\alpha^0(\theta_0)$ where θ_0 is an initial temperature.

The single crystal's constitutive description is completed with a specification of its elasticity, which is expressed in terms of $\mathbf{S}^* = \mathbf{F}^{*-1} \cdot \boldsymbol{\tau} \cdot \mathbf{F}^{*-T}$, the lattice-based second Piola–Kirchhoff stress, and $\mathbf{E}^* = \frac{1}{2}(\mathbf{F}^{*T} \cdot \mathbf{F}^* - \mathbf{I})$, the Green strain of the lattice, where $\mathbf{I}$ is the second-order identity tensor. Let $\Phi = \Phi(E_{ij}^*)$ be the Helmholtz free energy of the lattice per unit reference volume, and then

$$S_{ij}^* = \frac{\partial \Phi}{\partial E_{ij}^*}; \qquad \mathbf{S}^* = S_{ij}^* \mathbf{a}_i \mathbf{a}_j; \qquad \mathbf{E}^* = E_{ij}^* \mathbf{a}_i \mathbf{a}_j, \qquad (9)$$

where the time-independent Cartesian base vectors $\mathbf{a}_i$ are aligned with the crystal lattice in the reference configuration in some standard way. Differentiation of the first of (9) with respect to time gives the rate form

$$\left. \begin{aligned} \dot{\mathbf{S}} &= \mathbf{K} : \dot{\mathbf{E}}^*, \qquad \mathbf{K} = K_{ijkl} \mathbf{a}_i \mathbf{a}_j \mathbf{a}_k \mathbf{a}_l, \\ K_{ijkl} &= \frac{\partial^2 \Phi}{\partial E_{ij}^* \, \partial E_{kl}^*}. \end{aligned} \right\} \qquad (10)$$

In practice, it is usually sufficient to use the isotropic linear elasticity K_{ijkl} and doing so makes the assumption that the lattice is unaffected by plastic slip.

The final constitutive theory is expressed in terms of the second Piola–Kirchhoff stress, $\mathbf{S} = \mathbf{F}^{-1} \cdot \boldsymbol{\tau} \cdot \mathbf{F}^{-T}$, and the Green (or Lagrangian) strain, $\mathbf{E} = \frac{1}{2}(\mathbf{F}^T \cdot \mathbf{F} - \mathbf{I})$. Straightforward manipulation of the above equations give the rate form of the governing constitutive equation,

$$\dot{\mathbf{S}} = \mathbf{L} : \dot{\mathbf{E}} - \dot{\gamma}_\alpha \mathbf{X}_\alpha - \dot{\theta} \mathbf{Y}, \qquad (11)$$

where

$$\left. \begin{aligned} L_{ijrn} &= \hat{F}_{ik}^{-1} \hat{F}_{jl}^{-1} K_{klpq} \hat{F}_{rp}^{-1} \hat{F}_{nq}^{-1} \\ \mathbf{L} &= L_{ijkl} \mathbf{a}_i \mathbf{a}_j \mathbf{a}_k \mathbf{a}_l, \qquad \hat{\mathbf{F}}^{-1} = \hat{F}_{ij}^{-1} \mathbf{a}_i \mathbf{a}_j, \end{aligned} \right\} \qquad (12)$$

and

$$\left. \begin{aligned} \mathbf{X}_\alpha &= \hat{\mathbf{F}}^{-1} \cdot (\mathbf{K} : \mathbf{A}_\alpha + 2\mathbf{H}_\alpha) \cdot \hat{\mathbf{F}}^{-T}, \\ \mathbf{Y} &= \hat{\mathbf{F}}^{-1} \cdot (\mathbf{K} : \mathbf{B} + 2\mathbf{Q}) \cdot \hat{\mathbf{F}}^{-T}, \\ \mathbf{A}_\alpha &= \mathrm{sym}\, [\mathbf{F}^{*T} \cdot \mathbf{F}^* \cdot \mathbf{F}^\theta \cdot (\mathbf{s}_\alpha \mathbf{m}_{(\alpha)}) \cdot \mathbf{F}^{\theta-1}], \\ \mathbf{H}_\alpha &= \mathrm{sym}\, [\mathbf{F}^\theta \cdot (\mathbf{s}_\alpha \mathbf{m}_{(\alpha)}) \cdot \mathbf{F}^{\theta-1} \cdot \mathbf{S}^*], \\ \mathbf{B} &= \mathrm{sym}\, (\mathbf{F}^{*T} \cdot \mathbf{F}^* \cdot \boldsymbol{\alpha}), \qquad \mathbf{Q} = \mathrm{sym}\, (\boldsymbol{\alpha} \cdot \mathbf{S}^*). \end{aligned} \right\} \qquad (13)$$

The constitutive theory has been implemented into our finite-element code, where the details will be shown in § 2.2. Although the model has the ability to deal with more

complex problems including temperature variation and/or non-Schmid effects, the present problem only deals with isothermal deformations without any non-Schmid effects. Thus, explicit references to temperature and non-Schmid terms are neglected henceforth.

2.2. *Finite-element implementation*

The rate constitutive equations, notably (11), are implemented by the one step, explicit rate tangent method introduced by Pierce *et al.* (1983). The time discrete form of the relations that derived from the algorithm is given by

$$\dot{\mathbf{S}}^t = \mathbf{L}^{\text{tan}} : \dot{\mathbf{E}}^t - \mathbf{X}^{\text{tan}}, \tag{14}$$

where $\mathbf{L}^{\text{tan}}$ and $\mathbf{X}^{\text{tan}}$ are determined explicitly from the state at time t. The above rate form is then implemented in a finite element context via the principle of virtual work. In order to enforce the equilibrium at the end of the time step, we take the principle of virtual work as

$$\int_V \mathbf{n}^{t+\Delta t} : \delta \mathbf{F} \, \mathrm{d}V = \int_S \mathbf{t}^{t+\Delta t} \cdot \delta \mathbf{u} \, \mathrm{d}S, \tag{15}$$

where the body force is ignored. The integration is over the reference volume V, whose surface is S. $\mathbf{t} = \mathbf{N} \cdot \mathbf{n}$ is the nominal traction, where $\mathbf{N}$ is the outward unit normal to surface S, $\mathbf{n} = \mathbf{F}^{-1} \cdot \tau = \mathbf{S} \cdot \mathbf{F}^{\text{T}}$ is the nominal stress and $\delta \mathbf{u}$ is an admissible variational displacement field that is compatible with the variational deformation gradient field, $\delta \mathbf{F}$. To obtain the evolution of the solution through time, the explicit difference relation $\mathbf{n}^{t+\Delta t} = \mathbf{n}^t + \dot{\mathbf{n}}^t \Delta t$ is substituted into (15), which gives

$$\int_V [\delta \mathbf{E} : \mathbf{L}^{\text{tan}} : \dot{\mathbf{E}}^t + [\mathbf{S}^t \cdot (\dot{\mathbf{F}}^t)^{\text{T}}] : \delta \mathbf{F}] \, \mathrm{d}V = \int_V \left(\dot{\mathbf{X}}^{\text{tan}} - \frac{1}{\Delta t} \mathbf{S}^t \right) : \delta \mathbf{E} \, \mathrm{d}V + \frac{1}{\Delta t} \int_S \mathbf{t}^{t+\Delta t} \cdot \delta \mathbf{u} \, \mathrm{d}S. \tag{16}$$

Further details regarding (16) can be found in Dève, Harren, McCullough and Asaro (1988).

The time discrete variational equation is then written in Cartesian indexical form on the reference base vectors $\mathbf{a}_i$. Then the usual finite element interpolation and gradient operators are introduced to obtain a linear system of equations. After applying the appropriate rate boundary conditions and solving the resulting linear system of equations. The state at time $t + \Delta t$ is calculated and updated from the state at time t.

§3. POLYCRYSTAL MODEL

Realistic, three-dimensional finite element polycrystal analyses would require very large amounts of computer memory and CPU time. In order to study the deformation and failure modes in TiAl polycrystals, a two-dimensional idealization is made. The idealization scheme is inspired by the previous two-dimensional idealizations made by Harren *et al.* (1988), Harren and Asaro (1989) and McHugh *et al.* (1993) originally intended for f.c.c. or b.c.c. polycrystals and their metal matrix composites.

3.1. *Two-dimensional poly-synthetically twinned single crystal modelling*

The essential prerequisite to modelling the anisotropic macroscopic deformation and inhomogeneities is to include the essential microscopic slip and/or twinning

B. K. Kad *et al.*

deformation modes of the constituent phases into the aggregate theory. The slip system geometry and crystallography of the α_2 and γ constituent phases of the real three-dimensional PST material are shown in fig. 5 (a)–5 (d). The slip systems in order of increasing CRSS in α_2-Ti$_3$Al phase are (i) $\langle11\bar20\rangle\{10\bar10\}$ prism slip system with a $\tau_{crit}\approx100\,\mathrm{MPa}$, (ii) $\langle11\bar20\rangle(0001)$ basal slip system with $\tau_{crit}\approx330\,\mathrm{MPa}$, and (iii) $\langle11\bar26\rangle\{11\bar21\}$ pyramidal slip system with $\tau_{crit}\approx910\,\mathrm{MPa}$. The slip systems in the γ-TiAl phase, in order of increasing CRSS are (i) $\langle1\bar10]\{111\}$ perfect dislocation slip system, (ii) $\langle011]\{111\}$, and (iii) $\langle112]\{111\}$ superdislocation slip systems. In lamellar alloys, three different deformation modes are possible:

(i) Soft mode: lamellae oriented at about 45° to the loading axis. Deformation occurs in the soft γ-phase with deformation vectors parallel to the lamellar interface. No constraints are exerted by the α_2-phase. Soft mode resistance is affected by colony/domain size.

(ii) Intermediate mode: lamellae oriented nearly parallel to the loading axis. Deformation occurs in the soft γ-phase with deformation vectors parallel to the lamellar interface, but gliding on the cross-slip planes. In this configuration, the maximum constraint exerted by the α_2-phase is determined by the

Fig. 5

(a) $\qquad\qquad\qquad\qquad\qquad$ (b)

(c) $\qquad\qquad\qquad\qquad\qquad$ (d)
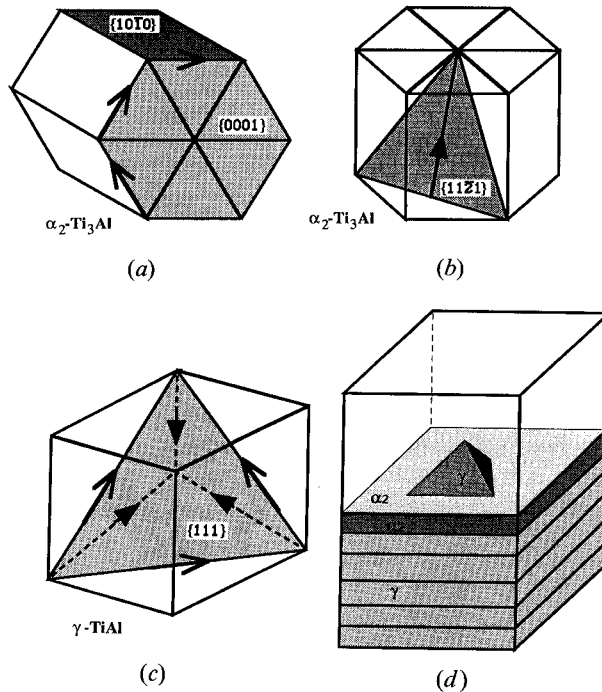
Three-dimensional slip system geometry of the $\alpha_2+\gamma$ constituent phases, and crystallography of the composite mix. (a) Soft mode $\langle11\bar20\rangle\{10\bar10\}$ prism and $\langle11\bar20\rangle(0001)$ basal slip systems in α_2-Ti$_3$Al. (b) Hard mode $\langle11\bar26\rangle\{\bar1\bar121\}$ pyramidal slip system in α_2-Ti$_3$Al. (c) Soft mode (open arrows) and hard mode (solid arrows) octahedral slip systems in γ-TiAl. (d) Schematic of the laminate geometry indicating the soft mode slip plane (shaded region) as the interface plane between γ-TiAl and α_2-Ti$_3$Al. The orientation relationship is $(0001)\alpha_2\|\{111\}\gamma$ and $\langle11\bar20\rangle\alpha_2\|\langle1\bar10\rangle\gamma$.

Fig. 6
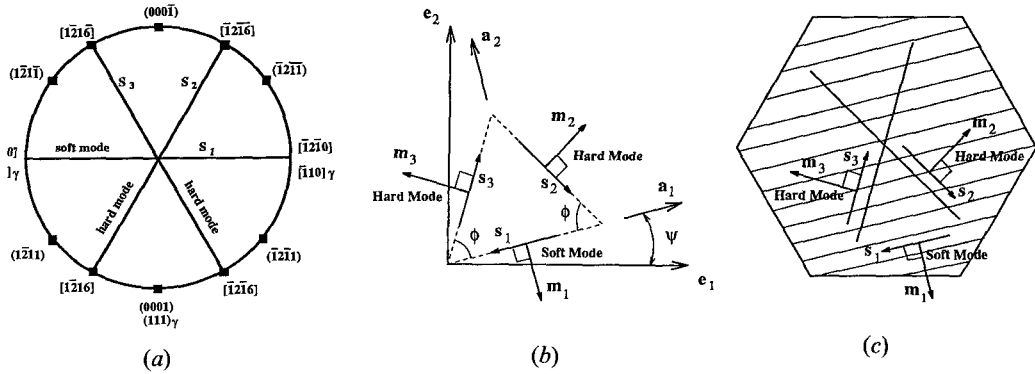
Two-dimensional (2D) schematic of the soft and hard mode slip systems in the laminate morphology. (*a*) Projected two-dimensional slip systems; $\tau_1 = \tau_{\text{soft-mode}}$ derived from shear in γ-TiAl parallel to the laminates and $\tau_2 = \tau_3 = \tau_{\text{hard-mode}}$ derived from the $\langle 11\bar{2}6 \rangle \{11\bar{2}1\}$ pyramidal slip system constraint imposed by the harder α_2-Ti$_3$Al phase. $\{\bar{1}010\}$ projection of α_2-Ti$_3$Al, incorporating the lamella normal in the plane of the sample for the 2D approximation. Only in-plane Burgers vectors are considered in the 2D model. (*b*) Final construction of the input slip-system morphology for the 2D model. (*c*) Embedding the projected 2D slip geometry into the single crystal lamellar morphology.

stress required to activate $\langle 11\bar{2}0 \rangle \{10\bar{1}0\}$ prism slip, which is nearly equal to 100 MPa. Intermediate mode resistance is affected by colony/domain size.

(iii) Hard mode: lamellae oriented nearly perpendicular to the loading axis. Maximum constraint exerted by the α_2-phase is determined by the stress required to activate the $\langle 11\bar{2}6 \rangle \{11\bar{2}1\}$ pyramidal slip; this involves a $\tau_{\text{crit}} \approx 910$ MPa. This constraint is, however, strongly scale (i.e. lamellar thickness) dependent.

In an effort to reduce the processing time, certain simplifying assumptions were made to reduce the problem to a two-dimensional plane strain simulation. Figure 6 (*b*) shows the reference configuration of the two-dimensional PST model used throughout in our theoretical simulations. In this two-dimensional reference configuration, we replace the three-dimensional crystallographic slip system input with a projected two-dimensional input such that the lamellar normals are configured to lie in-plane and only in-plane slip vectors are considered (fig. 6 (*a*)). The three slip systems of the single PST are arranged in a non-equilateral triangle, and the reference crystal base vectors $\mathbf{a}_i$ are aligned with the crystal lattice as shown. Slip system $(\mathbf{s}_1, \mathbf{m}_1)$ is the soft mode slip system; $(\mathbf{s}_2, \mathbf{m}_2)$ and $(\mathbf{s}_3, \mathbf{m}_3)$ are equivalent hard mode slip systems. Angle $\phi = 58°$. We use the soft and the hard mode τ_{crss} values as described earlier (Yamaguchi and Umakoshi 1991). In the two-dimensional model, the embedded geometry (fig. 6 (*c*)) is based on the composite γ-TiAl + α_2-Ti$_3$Al mixture. Thus, the soft mode slip system $(\mathbf{s}_1, \mathbf{m}_1)$, is ascribed to the γ-TiAl phase, the hard mode slip systems $(\mathbf{s}_2, \mathbf{m}_2)$ and $(\mathbf{s}_3, \mathbf{m}_3)$ are ascribed to the α_2-Ti$_3$Al phase. This explains the angle $\phi = 58°$ as being the projection of the $\langle 11\bar{2}6 \rangle \{11\bar{2}1\}$ pyramidal system (in α_2) as projected in two dimensions, see fig. 6 (*b*). In the current context, we

have constructed our input employing only two unique slip systems in an isosceles triangle. The model however, may incorporate three unique inputs, as might be required for non-equivalent slip systems (i.e., varying CRSS and hardening parameters), particularly in non-cubic crystal structures. For example, the $\langle 11\bar{2}0\rangle\{10\bar{1}0\}$ prism slip, $\langle 11\bar{2}0\rangle(0001)$ basal slip, and $\langle 11\bar{2}6\rangle\{11\bar{2}1\}$ pyramidal slip system in the α_2-Ti$_3$Al phase may be represented by an asymmetrical triangle of input slip system geometry. Finally, in the specific example of lamellar TiAl, the model does not specify initial orientations about the lamella normal, since the yield stress is essentially constant for any such rotations (Fujiwara et al. 1990).

3.2. Input data for two-dimensional idealization

The single crystal (colony) data for two-phase $\alpha_2 + \gamma$ lamellar alloys has been extracted for (i) tension (Inui et al. 1992), (ii) compresson (Fujiwara et al. 1990), and (iii) for varying lamella thickness (Umakoshi et al. 1991). The γ-TiAl single crystal data is extracted from Kawabata, Kanai and Izumi (1986).

   (i) Fully lamellar material:
      τ_{crss} (soft-mode) $= g_1^0 = 50\text{–}75$ MPa,
      soft mode hardening rate $= h_{11} = 150$ MPa,
      τ_{crss} (hard-mode) $= g_2^0 = g_3^0 = 300,\ 600,\ 900,\ 1200$ MPa,
      hard mode hardening rate $= h_{22} = h_{33} = 1500$ MPa.
   (ii) Nearly lamellar $+ 4$ and 12 vol.% γ-TiAl:
      τ_{crss} (duplex-γ) $= 85$ MPa,
      duplex γ hardening rate $= 1500$ MPa.

The Hall–Petch correlations provide a somewhat simple comparison between scale independent modelling predictions and experimental observations. Thus for any given microstructure, the soft mode is determined by the grain size (more appropriately the domain size) and the hard mode is determined by the individual thickness of slabs (cooling rate effect) and the volume fraction of α_2 (composition effect). These details of domain size and lamella thickness in single colonies (i.e., colony/grain size $= G$), as they affect $\tau_{\text{crss}}^{\text{soft}}$, $\tau_{\text{crss}}^{\text{hard}}$ parameters in the polycrystalline aggregate (for grain size $= G$) is illustrated schematically in fig. 7. In all cases the soft mode ($\tau_{\text{crss}}^{\text{soft}}$) is

Fig. 7

G = Grain size
D = Domain size
L = Lamellar width
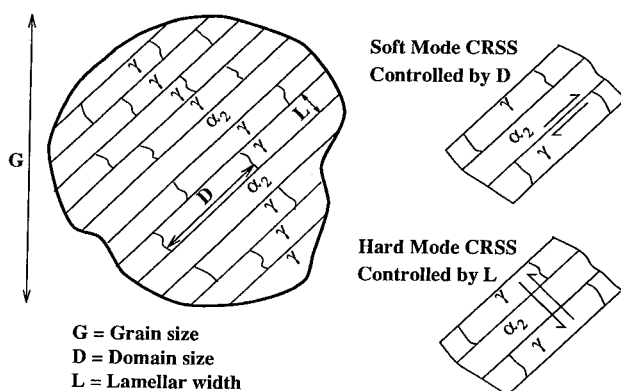
Soft and hard shear deformation modes as embedded in the model microstructure.

virtually independent of α_2 and shows little variation (maximum 50%) even for domain size effect. Thus, the soft mode yield strength varies from ≈ 75–150 MPa for a domain size variation of 500–$10\,\mu m$ (Nakano *et al.* 1992), respectively.

Initial simulations are thus made at discrete values of τ_{crss} (soft mode) and τ_{crss} (hard mode) (thereby accounting for microstructural scaling effects) to identify the range of the flow curves as observed experimentally.

The simulated tests are performed at a strain rate $1 \times 10^{-3}\,s^{-1}$, consistent with the range of testing strain rates commonly employed to generate the experimental data, such as that shown in fig. 3 (*a*); the reference shear rate $\dot{a}$ in eqn. (7) is taken as $1 \times 10^{-3}\,s^{-1}$. Additionally the material strain rate sensitivity exponent m is taken as 0·005, in accordance with the experimentally observed low strain rate sensitivity in the $2 \times 10^{-3}\,s^{-1}$ to $1 \times 10^{-4}\,s^{-1}$ range (see Mendiratta, Kim and Dimiduk (1993)). The elastic moduli are taken to be $\lambda = 69\cdot7$ GPa and $\mu = 71\cdot4$ GPa (Lipsitt, Shechtman and Schafrik 1975) for the lamellar TiAl single crystals in our computations.

3.3. *Polycrystalline modelling*

The reference configuration of the two-dimensional single crystal model was shown earlier, fig. 6 (*b*). The three slip systems of the single crystal are arranged in a triangle, and the reference crystal base vectors $\mathbf{a}_i$ are aligned with the crystal lattice as shown. Reference laboratory base vectors $\mathbf{e}_i$ are at an angle ψ with respect to reference crystal base vectors $\mathbf{a}_i$. In the $\alpha_2 + \gamma$ lamellar structure, slip system $(\mathbf{s}_1, \mathbf{m}_1)$ is the soft mode slip system; slip systems $(\mathbf{s}_2, \mathbf{m}_2)$ and $(\mathbf{s}_3, \mathbf{m}_3)$ are equivalent hard mode slip systems, where $\phi = 58°$. For bulk γ-TiAl single crystals, slip systems $(\mathbf{s}_1, \mathbf{m}_1)$, $(\mathbf{s}_2, \mathbf{m}_2)$ and $(\mathbf{s}_3, \mathbf{m}_3)$ are taken as equivalent slip systems, where $\phi = 60°$.

Since the material response would depend largely on the plastic property of the crystals, we take the elasticity to be isotropic, where Lame's constant λ and elastic shear moduli μ are used. Deformations are assumed to be isothermal so that explicit reference to temperature is omitted. The lattice is assumed to deform in plain strain. The hardening is a simple linear hardening, with no latent hardening. The hardening matrix $h_{\alpha\beta}$ is given as:

$$\left. \begin{array}{l} h_{11} = \text{soft mode hardening rate}, \qquad h_{22} = h_{33} = \text{hard mode hardening rate}, \\ h_{ij} = 0 \; (i \neq j). \end{array} \right\} \quad (17)$$

The reference configuration of the two-dimensional polycrystal microstructure to be analysed is shown in fig. 8, where the Cartesian base vectors $\mathbf{e}_i$ describe the orientation of the polycrystal's reference configuration with respect to the laboratory. Each of the 27 grains (or single PSTs) indicated in fig. 8 (*a*) is defined by an orthogonal transformation $\mathbf{a}_i^n = \psi_{ij}(\psi^n)\mathbf{e}_j$, $n = 1, \ldots, 27$, where ψ^n is the angle ψ shown in fig. 6(*b*) for the *n*th grain. Since a symmetry operation for each grain is a 180° rotation about $\mathbf{e}_3$ axis, a random value between 0° and 180° was assigned to each grain with respect to $\mathbf{e}_3$. Without losing any generality, we take the angles to be integral degrees. Note that it would be straightforward to include pre-texturing with the model. In any event the aggregate will develop texture as a natural outcome of the deformation process.

The finite element mesh used in the polycrystal calculations consisted initially of rectangular 'crossed-triangle' quadrilateral elements in a uniform grid 40 rectangles wide by 56 rectangles high, which is 8960 constant strain triangles totally, fig. 8 (*b*). No geometric imperfections was present in the initial mesh. The mesh dimensions were chosen to represent equiaxed grains. Finally, all of the grain boundaries in this

Fig. 8
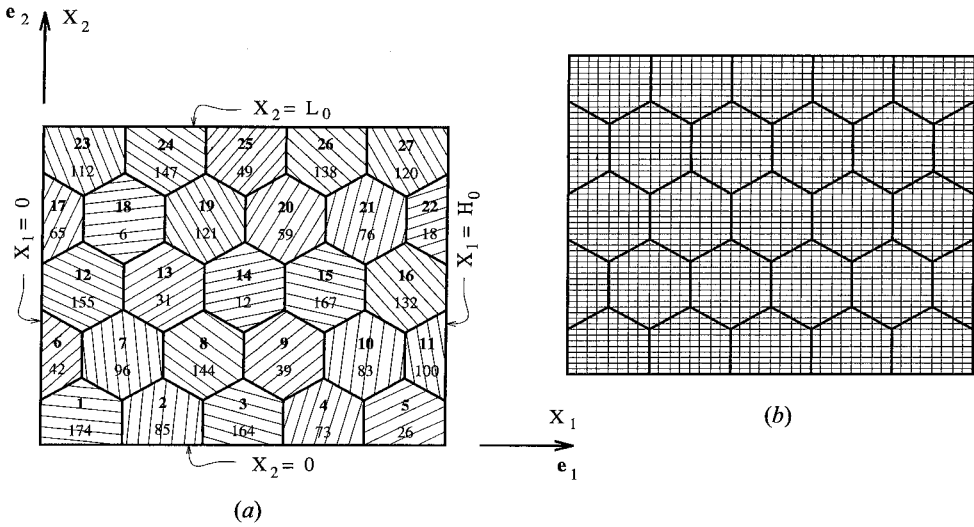
(*a*) Reference configuration of the 27 lamellar crystals representing the randomly generated polycrystalline aggregate. The orientations ψ^n shown are selected in the $180° \geqslant \psi^n \geqslant 0°$ range. (*b*) The finite element mesh consists of 8960 constant strain triangles in a uniform grid of 40×56 rectangular 'crossed-triangle' quadrilateral elements. No geometric imperfections are present in the initial mesh and the grain boundaries in this polycrystal model coincide with either an edge or a diagonal of a quadrilateral element, i.e. with an edge of a constant strain triangle.

polycrystal model coincide with either an edge or a diagonal of a quadrilateral element, i.e. with an edge of a constant strain triangle.

As stressed by Harren *et al.* (1988), the grain boundaries are 'continuum grain boundaries'. This is a continuum theory, and that the polycrystal's initial reference configuration is assumed to be stress free and without any lattice perturbations. In fact each grain boundary is a line across which the initial lattice orientation ψ^n has a jump.

The loading histories that will be described here are constrained to be orthotropic, but looking at the polycrystal's reference configuration in fig. 8 (*a*), there is no special symmetry for this aggregate and one would not expect it to deform in an orthotropic manner. Nevertheless, we take this aggregate as a material 'point' in a polycrystal material, and take a Taylor-like assumption that the deformation gradient of this aggregate (which is represented by the four straight lateral boundaries) is the same as the global deformation gradient. For the simple tension and compression tests, we have the boundary conditions set to be

$$
\left.
\begin{aligned}
\dot{u}_2(X_1, 0) &= 0, & \dot{t}(X_1, 0) &= 0, \\
\dot{u}_1(0, X_2) &= 0, & \dot{t}_2(0, X_2) &= 0, \\
\dot{u}_1(H_0, X_2) &= \dot{U}_1, & \dot{t}_2(H_0, X_2) &= 0, \\
\dot{u}_2(X_1, L_0) &= \dot{U}_2, & \dot{t}_1(X_1, L_0) &= 0.
\end{aligned}
\right\}
\tag{18}
$$

Here, $\dot{\mathbf{u}} = \dot{u}_i \mathbf{e}_i$ is the material particle velocity, $\dot{\mathbf{t}} = \dot{t}_i \mathbf{e}_i$ is the rate of nominal traction, i.e. $\dot{\mathbf{t}} = \mathbf{N} \cdot \dot{\mathbf{n}}$ ($\mathbf{N}$ is the outward unit normal to the aggregate boundaries), $\dot{U}_1$ is the normal velocity on the material face $X_1 = H_0$ and $\dot{U}_2$ is the normal velocity on the material face $X_2 = L_0$. Also, the total loads on the unit cell (polycrystal aggregate) in X_1 and X_2 directions are, respectively,

$$P_1 = \int_0^{L_0} t_1(H_0, X_2) \, dX_2, \qquad P_2 = \int_0^{H_0} t_2(X_1, L_0) \, dX_1. \qquad (19)$$

The prescription for boundary value problem is completed by setting $\dot{P}_1 = 0$ and $(\dot{U}_2/L_0) = \dot{a}$ for tension or $(\dot{U}_2/L_0) = -\dot{a}$ for compression, and hence $\dot{U}_1$ and $\dot{P}_2$ are unknowns to be solved during the course of the solution of the rate boundary value problem. The initial state of this problem corresponds to zero stress and zero strain.

To account for small volume fraction of γ-TiAl phase, located at the grain boundaries owing to the heat-treatments, second phase 'corner grains' were constructed, as illustrated in fig. 9. The corner morphologies with 4 vol.% and 12 vol.%

Fig. 9

(a)   (b)

(c)
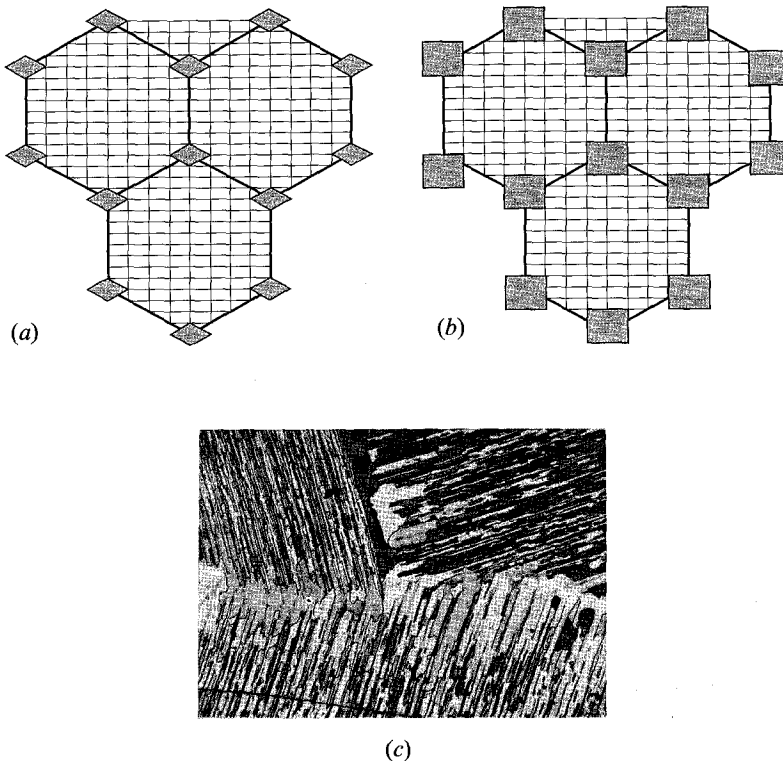
Construction of 'grain corners' of equi-axed γ-TiAl, as precipitated from the α-phase on heat treatment for nearly lamellar (NL) microstructures; (a) 4 vol%, (b) 12 vol% and (c) actual microstructure of the lamellar geometry obtained by continuous cooling through the $\alpha + \gamma$ phase field. Specific detail of the microstructure in the vicinity of the triple point is of interest.

second phase 'corner grains' are shown in fig 9 (*a*) and 9 (*b*) respectively. For each of these γ-TiAl corner grains, ψ is assigned a random orientation angle $0° \leqslant \psi \leqslant 60°$.

§ 4. RESULTS AND DISCUSSION

In what follows, we have attempted to compare our model simulations with an available experimental data base for polycrystalline alloys, see fig. 3 (*a*). This particular data set is representative of the general cross-section of room temperature (RT) mechanical behaviour, and allows for an evaluation of thermomechanical processing effects, without concern over the variability of chemistry and processing procedure from one data set to another. A few 'proof of concept' experiments were conducted to corroborate the specific material behaviour predicted by the simulations.

Four different representations of the computational results are presented. These are (i) the computed stress–strain response of the polycrystalline aggregate, (ii) accumulated strain patterns in the deformed microstructures at finite macroscopic strains which illustrate the localization of deformation, (iii) highly non-uniform lattice rotations in the deformed microstructure at finite macroscopic strains, and (iv) the evolution of hydrostatic stresses in the deformed microstructures at finite macroscopic strains. Since polycrystalline specimens typically fail at about 2–4% strain in tension, the simulations are terminated at 5% overall strain.

4.1. *Single against (fully lamellar) polycrystal simulations*
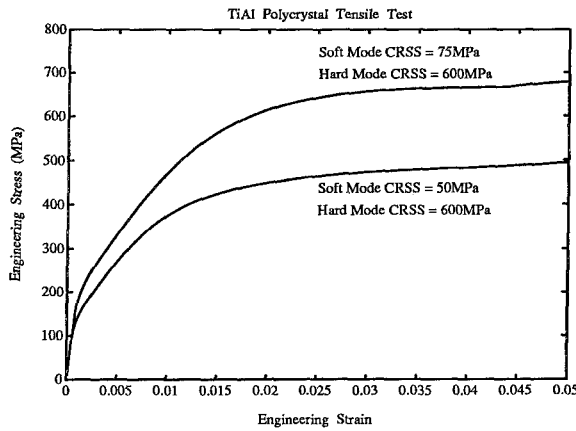4.1.1. *Tensile flow stress behaviour*

Figure 10 shows computed stress against strain behaviour for the two-dimensional model microstructure described in fig. 8. For each of the simulated flow curves in fig. 10 (*a*), the soft mode initial critical resolved shear stress (g_1^0) is fixed at 50 MPa, and the hard mode initial critical resolved shear stress $(g_2^0 = g_3^0)$ varied from 300–1200 MPa in increments of 300 MPa. This range of g_2^0 $(= g_3^0)$ values spans reported experimental values (Inui *et al.* 1992, Nakano *et al.* 1992), and corresponds approximately (through the Hall–Petch parameter) to lamella thicknesses in the range 4·90 μm–0·16 μm (Nakano *et al.* 1992). Figure 10 (*b*) shows a second simulation for the two-dimensional model microstructure. For the simulated flow curves, the hard mode initial critical resolved shear stress $(g_2^0 = g_3^0)$ is fixed at 600 MPa and the soft mode initial critical resolved shear stress (g_1^0) is 50 and 75 MPa corresponding to domain sizes of approximately 60 and 10 μm respectively. The work hardening behaviour beyond about 1% strain is essentially constant, in concert with experimental data (Kim 1992) and is achieved by fixing the hard mode strain hardening rate (i.e. h_{22} and h_{33}) at 1500 MPa as extracted from the experimental data on single crystals (Nakano *et al.* 1992). The effect of individually increasing the hard mode strain hardening rate to 3000 MPa is very small, and is not pursued further.

The numerical computations accurately span the experimentally observed plastic behaviour in lamellar microstructures as shown in fig. 3 (*a*). Matching in the elastic regime is poor on account of the limited initial constraints in the two-dimensional idealization resulting in a Taylor factor that is lower than for three-dimensional polycrystal. Despite the two-dimensional idealization, the underlying deformation mechanisms for the polycrystalline lamellar TiAl microstructures are well captured. Therefore, using single crystal properties as input parameters, one would expect the predicted response of this two-dimensional model microstructure corresponds well

Fig. 10
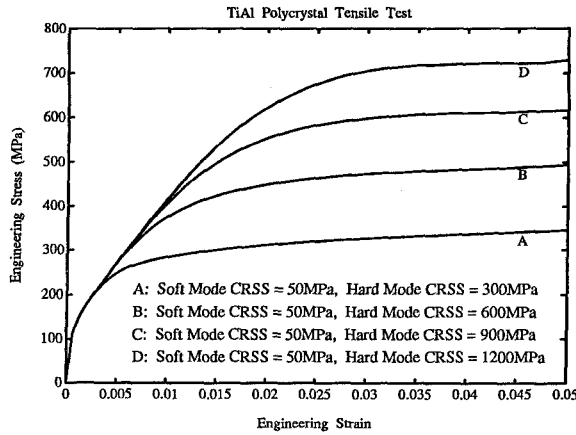
(a)

(b)

Computed stress–strain behaviour for the two-dimensional model microstructure constructed in fig. 8. (*a*) For each of the simulated flow curves *A*, *B*, *C*, *D*, the soft mode stress $(g_1^0) = 50$ MPa and the hard mode stress $(g_2^0 = g_3^0)$ varied from 300–1200 MPa in increments of 300 MPa each for curves *A*, *B*, *C*, *D*, respectively. (*b*) For the simulated flow curves 1, 2, the hard mode stress $(g_2^0 = g_3^0) = 600$ MPa and the soft mode stress (g_1^0) is 50 and 75 MPa, respectively.

with reality. For the particular data set used for comparison purposes here (Kim 1992), we are simulating changes in the soft mode CRSS. For example, in the experimental flow curves *A*, *B*, *C* in fig. 3 (*a*), the grain size decreases from *A* to *B* to *C* (as a result of holding temperature and holding time) with corresponding increases in flow stress. Since the soft mode CRSS is inversely scaled with the domain size (or more appropriately, the grain size), this has the net effect of raising the input for soft mode CRSS, thereby effecting the increase in the theoretical flow curves, fig. 10 (*b*). On the other hand since cooling rates are identical, see fig. 3 (*a*), the hard modes stresses ought to be equivalent.

The relationship between domain size and colony size deserves special attention. Domain boundaries are present in polycrystalline microstructures and so a specific need is to determine a relationship between domain size and grain size. Domain boundary hardening associated with slip transmission depends on the APB energy term (Kad *et al.* 1993) and is a minor effect, as manifested in a small Hall–Petch parameter (Nakano *et al.* 1992). Thus, τ_{crss}^{soft} varies from 38–75 MPa for domain size variations of 600–10 µm, respectively. In sharp contrast, the grain boundaries in polycrystalline materials contribute a much higher strengthening as manifested in a large Hall–Petch parameter (Kim 1993). Thus, one interpretation may be to use a given colony (grain) size as the maximum allowable domain size, and to simply scale the domain size with grain size. This sounds plausible as the entire range of flow stress curves from Kim's (1992) experimental data (for grain size range ≈ 10–1000 µm) is simulated by using a domain size variation of approximately 10–60 µm.

The two-dimensional model in its present form is scale independent. Thus, the Hall–Petch data for the soft and hard mode slip systems in single crystals is the most reliable way of accounting for domain size, grain size, and lamella width variations. The lamella widths primarily affect the hard mode, whereas, the domain size and grain size collectively affect the soft mode. The hard mode input is simply read off from the Hall–Petch data for a given lamella scale. However, our soft mode input CRSS does not, and cannot, distinguish between domain size or grain size effect and is a single input reflecting both grain size and/or domain size variations. It suffices to say that the range of single crystal inputs employed, and the rather simple two-dimensional idealization, are successful in predicting the range of flow stresses observed experimentally.

Based on these initial simulations, the input data sets A (soft mode CRSS $g_1^0 = 50$ MPa, hard mode CRSS $g_2^0 = g_3^0 = 600$ MPa) is inferred as the best combination of soft-mode, hard-mode CRSS input values and is the base reference for all further computations of inhomogeneous strain accumulations and stress distributions. Two additional data sets B (soft mode CRSS $g_1^0 = 75$ MPa, hard mode CRSS $g_2^0 = g_3^0 = 600$ MPa) and C (soft mode CRSS $g_1^0 = 50$ MPa, hard mode CRSS $g_2^0 = g_3^0 = 900$ MPa) are used, where necessary, to illustrate effects that may occur by altering soft mode CRSS (g_1^0), hard mode CRSS ($g_2^0 = g_3^0$) individually.

4.1.2. *Strain accumulations*

The accumulated strains in A (soft mode CRSS $g_1^0 = 50$ MPa, hard mode CRSS $g_2^0 = g_3^0 = 600$ MPa) at aggregate tensile strains of 1% and 5% are shown in fig. 11 (*a*) and 11 (*b*), respectively. For reasons of brevity and clarity, we first describe the generic features of the simulation at 1% strain for sample A. These features are best illustrated with reference to fig. 8 (*a*) where the shading in each PST crystal indicates its initial orientation. Regions of gross inhomogeneous deformation, both between and within grains, are immediately obvious. Maximum strains on the order of 14·5% occur at or near the grain boundaries, with particularly large concentrations at the triple points. This is illustrated by the large strains along the boundaries between crystal pairs 1–6, 4–5, 7–13, 19–25. The boundaries between crystals 12, 13, and 18 constitute the triple point strain localization of approximately 10% strain. Significant inhomogeneities are observed within the bulk of a single crystal. For example within each of the crystals 3, 4, 5, 12, 13, 16, 24, we observe strain accumulations vary from roughly zero to >5% strain. Within a given crystal, the direction of strain localizations (or deformation bands) are both parallel and perpendicular to the

Fig. 11
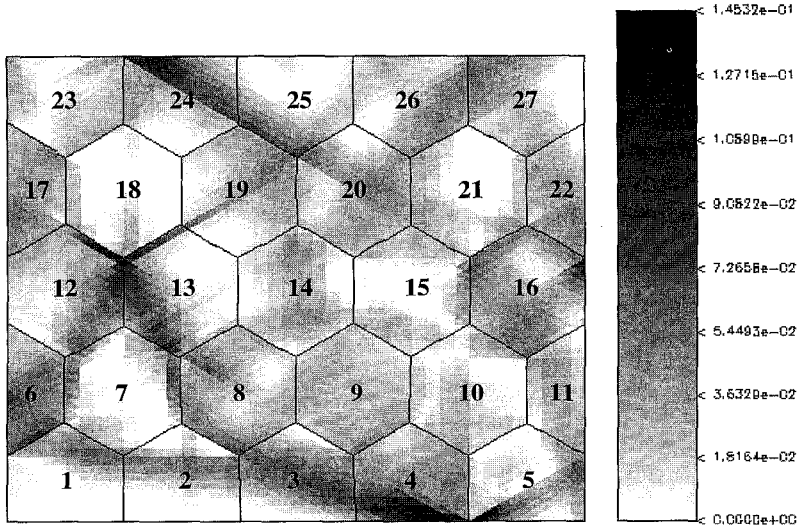
(*a*)
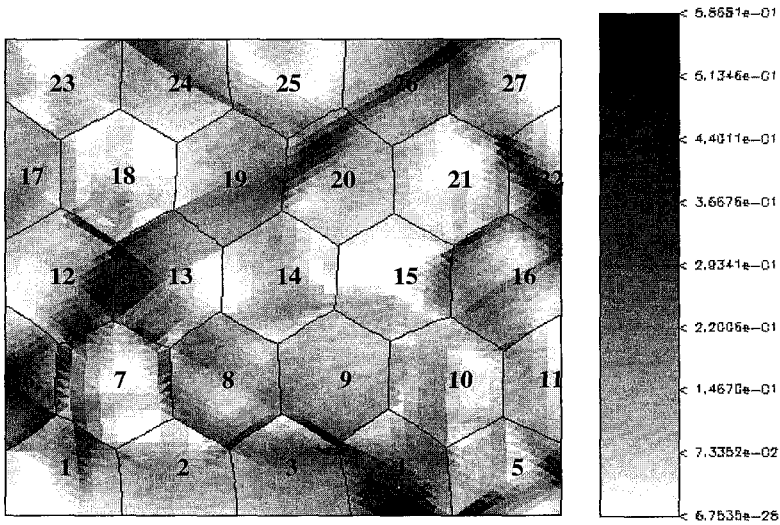
(*b*)

Contour of the accumulated sum of strains in the deformed two-dimensional model micro-structure at (*a*) 1%, and (*b*) 5% macroscopic strain. The data set is for ($g_1^0 = 50$ MPa, $g_2^0 = g_3^0 = 600$ MPa). Maximum localized strains are (*a*) 14·53% and (*b*) 58·68%.

laminates. For example the direction of strain localizations (or deformation bands) is parallel to the laminates in crystals 6, 8, 24, and perpendicular to the laminates in crystals 12, 25 and 26, see fig. 11 (*b*). Because of the soft-mode slip system parallel to the laminates, it is expected that strain localizations parallel to the soft mode will yield lower hydrostatic stress components. Strain localizations across the plate require

activation of hard mode slip systems, or cutting of the α_2 plates, and thus are considered as being additional constraining events requiring higher stress concentrations. This is discussed in the next section.

A peculiar characteristic of the crystals is their response to the varying nature of constraint at their boundaries. Note that excluding the affect of boundary conditions at the edges of the model microstructure, some of the most active strain accumulations occur in the vicinity of grain boundaries. These localizations occur as both parallel, see crystal pairs 3–9, 12–13, and perpendicular, see crystal pairs 20–26, 22–27, to the grain boundaries, see fig. 11. For example, in crystal 7, while the bulk of the crystal does not deform, small deformations are indeed observed close to the boundaries to comply with its more readily deformable neighbours. For example the strain is negligible across the boundary for crystal pair 2–7, but is about 5% across crystal pairs 6–7 and 7–8. In crystal 16, oriented for soft mode deformation, the strains at the boundaries are non-uniform, which is the result of the constraints by neighbouring crystals. Thus, the accumulated strain is about 5% at the triple point between crystals 15–16–21 and between crystals 10–11–16, but is almost 0% at triple point between crystals 10–15–16. Looking ahead to the next section, it will be shown that such non-uniform strains, in the vicinity of the grain boundaries, create large hydrostatic stresses. The mere instance of soft orientation does not in itself guarantee deformation in the soft γ-phase. For example, in crystals 12, 13 (both oriented in the soft mode) large portions of the crystals do not deform as they are constrained by their neighbours. The orientation dependent single crystal deformation behaviour is thus collectively affected by its neighbours, which in essence raises the flow stress.

Gross grain boundary deformations are evident along with some bending of the initial configuration of the boundaries at 5% aggregate strain, see fig. 11 (*b*). This aspect is dealt with in great detail in the next section. A small shear band (going from lower-left to upper right corner) begins to traverse through crystals 6, 7, 12, 13, 19, 20, and 26. In crystals 20, 26 this deformation band affects only half the crystal volume, such that variations in the strain accumulation within a crystal are clearly evident. Note that in crystal 20 the strain anisotropy is approximately parallel to the lamellae, which can be accomplished by delamination of either γ–γ plates, or γ–α_2 plates and slip parallel to the laminates either in the soft γ phase or at the 120° rotation interface.
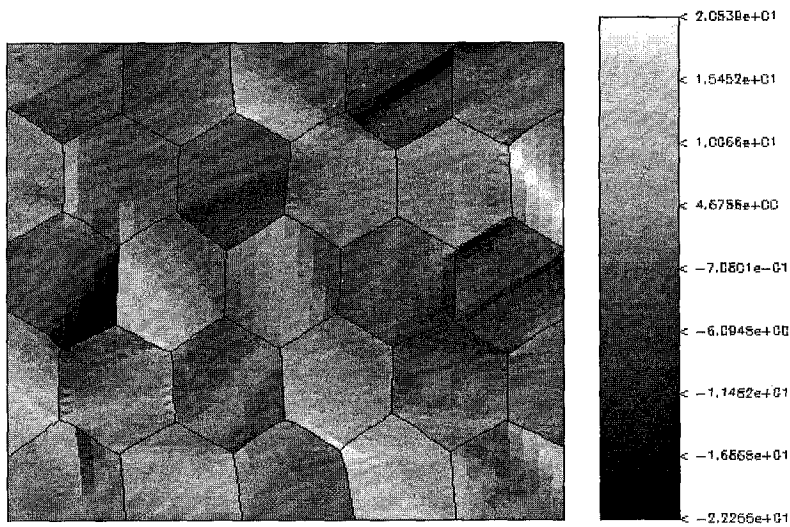
4.1.3. *Lattice rotations*

Non-uniform lattice rotations are yet another manifestation of the localization process described in the previous section. Figure 12 (*a*), 12 (*b*) show the maximum localized lattice rotations in the range 6° and 20° in A ($g_1^0 = 50\,\text{MPa}$, $g_2^0 = g_3^0 = 600\,\text{MPa}$) at aggregate tensile strains of 1% and 5%, respectively. Looking down the figure, positive rotations (see scale) are described in the anti-clockwise sense. The largest lattice rotations appear to be confined to the grain boundaries, analogous to the descriptions of the previous section. Thus, much of the detail presented here will appear reminiscent of the features elucidated in the previous section. For the sake of brevity, we only describe the essential features at 5% strain, see fig. 12 (*b*).

Lattice rotations are the natural consequence of the constrained crystallographic shearing process. The theoretical framework, within which such rotations are considered, was described previously, see fig. 4. Thus, with the exceptions of some grains on the periodic boundaries (i.e., crystals 4 and 22), the largest rotations are confined to crystals 6, 9, 12, 13, 16, 25, 26, deforming in the soft mode, i.e., those that dominantly contribute to the aggregate strain. Significant inhomogeneities are

Fig. 12
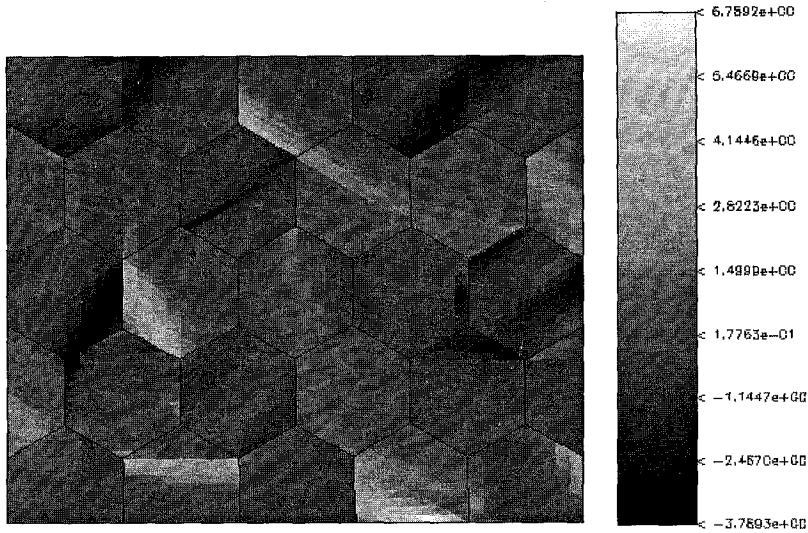
(a)

(b)

Contour of the lattice rotations in the deformed two-dimensional model microstructure at
(a) 1%, and (b) 5% macroscopic strain. The data set is for ($g_1^0 = 50$ MPa,
$g_2^0 = g_3^0 = 600$ MPa).

observed within the bulk of the crystal, for example crystals 9, 13, 22, 25, 26, and
across grain boundaries, for example between crystal pairs 3-9, 12-13, 16-21, 19-25.
In crystal 12 the rotations are largely clockwise, varying from about 1° at the upper
left to nearly 20° at the bottom right, close to the 6-12-13 triple point. In crystal 13,
the rotation is counterclockwise at bottom left, close to the 6-12-13 triple point, and

changes gradually to clockwise rotations of about 1-2° in the upper right corner. Looking back to the orientation of crystals 12 and 13, as described in fig. 8 (*a*), the rotation changes sign (or sense) about the lamella normal, a situation analogous to bending of the laminates. Looking ahead to the next section, we note both hydrostatic tension and compression components within the bulk of crystals 12 and 13. The localized rotations at triple points 6–12–13, and 12–13–18 are of particular interest. Considering the crystal pair 12–13 boundary, we note that large rotations (of about 20°) occur in the respective crystals across the boundary. The sense of rotations is opposite to one another (i.e., clockwise in crystal 13, anti-clockwise in crystal 12), such that the reltive rotation is about 40° compared to the undeformed microstructure. It appears intuitive that, crystals rotating in a sense opposite to their neighbours represent extreme incompatibilities, and are often accompanied by large hydrostatic stress as described in the next section. Finally, rotation localizations, close to the boundaries, appear to account for grain boundary shape changes, as observed at crystal pair boundaries 3–4, 22–27 and 24–25.
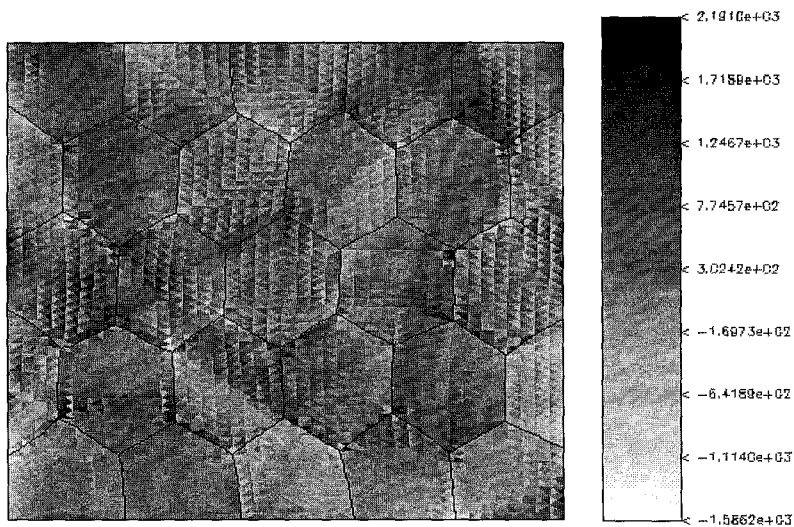
4.1.4. *Hydrostatic stresses*

Hydrostatic stresses developed in the simulations, i.e. corresponding to the strain accumulations shown in fig. 11 (*a*) and 11 (*b*) in sample material *A* at 1% and 5% aggregate strain are shown in fig. 13 (*a*) and 13 (*b*), respectively. For reasons of clarity several hydrostatic stress plots are constructed for stresses >500 MPa to better illustrate the localization sites of peak hydrostatic stresses. The inhomogeneous hydrostatic stress distribution, both between and within grains, is immediately obvious. For data set *A*, the flow stress at 1% strain is approximately 350 MPa. In sharp contrast, the peak hydrostatic stress developed is about 1200 MPa. The hydrostatic stress concentrations, with some exceptions, approximately parallel the inhomogeneous strain distributions (fig. 11 (*a*), 11 (*b*)) with the peak hydrostatic stresses existing at or near the grain boundaries, particularly the triple points. The hydrostatic stress distribution ranges from compressive to tensile, fig. 13 (*b*). For example, crystal 11 is experiencing mild compression, whereas crystals 2, 10, 27 are experiencing tension. Such fluctuations are observed as bands of tensile and compressive stresses traversing through the crystals. Thus tensile/compressive bipolar states are developed also within single crystals, as seen in crystals, 4, 5, 7 and 16. In particular the largest values of hydrostatic stresses, far exceeding the experimentally observed fracture stress (see fig. 3 (*a*)), are encountered at the boundaries and triple points, fig. 13 (*a*), 13 (*b*). For *A* (soft mode CRSS $g_1^0 = 50$ MPa, hard mode CRSS $g_2^0 = g_3^0 = 600$ MPa), the peak hydrostatic stresses >500 MPa developed (at the grain boundary/triple points) at 1% aggregate strain, are far in excess (≈ 1200 MPa) of the aggregate fracture stress reported by Kim (1992), see fig. 3.

The hydrostatic stresses may arise from (i) a large accumulation of strain, especially those activating hard mode slip and (ii) large deformation incompatibilities and lattice rotations between adjacent crystals. Thus, looking back to data set *A* in fig. 11 (*a*), 11 (*b*), incompatibilities at crystals 12–13–18, crystals 6–7, and crystals 7–8 yield large hydrostatic stress. In comparison, relatively smaller strain accumulations requiring hard mode activation in crystals 26, 27 also yield high hydrostatic stress. The hydrostatic stresses scale up with individual increases in the soft mode or hard mode CRSS values. When the increases in soft mode CRSS (g_1^0), hard mode CRSS ($g_2^0 = g_3^0$) are fractionally equivalent, the peak hydrostatic stresses are roughly similar, as shown in fig. 14 for *B* (soft mode CRSS $g_1^0 = 75$ MPa, hard mode CRSS $g_2^0 = g_3^0 = 600$ MPa) and *C* (soft mode CRSS $g_1^0 = 50$ MPa, hard mode CRSS $g_2^0 = g_3^0$

Fig. 13

(a)

(b)
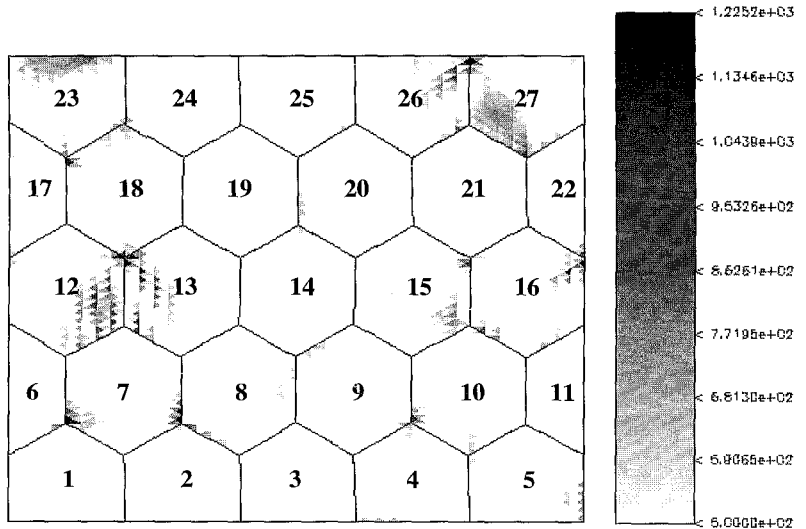
Contour of the hydrostatic stresses in the deformed two-dimensional model microstructure (corresponding to strain accumulations in fig. 11) at (a) 1%, and (b) 5% macroscopic strain. The data set is for ($g_1^0 = 50$ MPa, $g_2^0 = g_3^0 = 600$ MPa). Figure 13 (a) is constructed with hydrostatic stresses > 500 MPa, to better illustrate the localization of peak stresses at or near grain boundaries.

= 900 MPa), respectively at 5% macroscopic strain. Additionally, the hydrostatic stresses also scale up with aggregate strain approaching about 2200 MPa for A and about 3000 MPa for B and C data sets at 5% macroscopic strain. At these values they are, respectively, about three to five times the maximum observed fracture stresses in developmental lamellar or duplex alloys.

Fig. 14

(a)

(b)
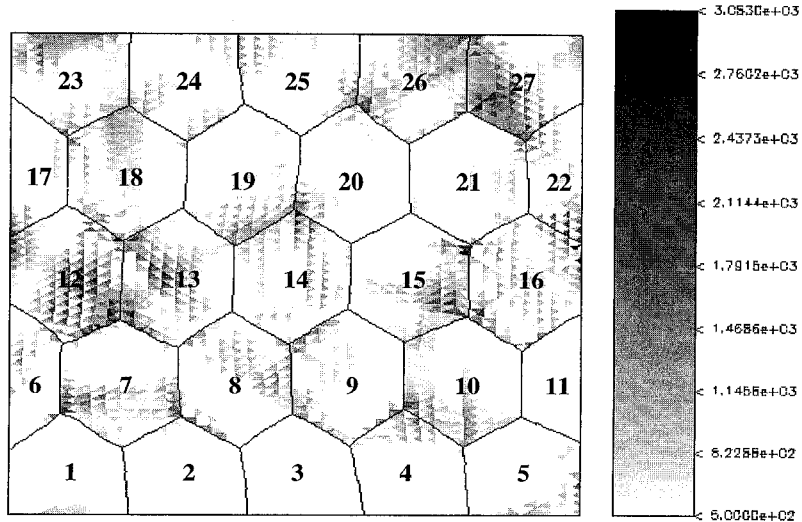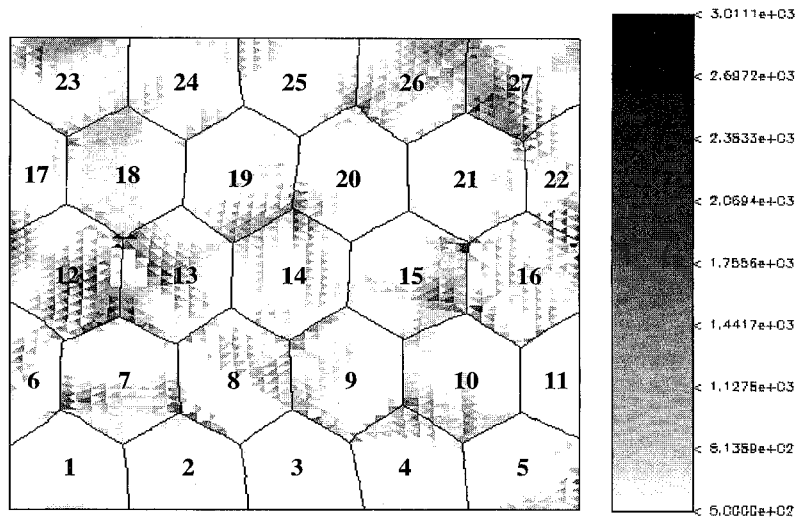
Contour of the hydrostatic stresses > 500 MPa in the deformed 2D model microstructure, at 5% macroscopic strain, for fractionally equivalent increases in (a) soft and (b) hard mode CRSS. The magnitudes of peak hydrostatic stresses are roughly similar.

The idea of intergranular/grain boundary cracking as being the origin of tensile failures in such laminated microstructures is not currently entertained in the literature. Though a myriad of fracture evidence of failed tensile segments is presented, one can only infer the general propagation path to failure, i.e., whether intergranular or transgranular? The sites of fracture initiation (or for that matter the

specific cause of failure) are not explicitly specified. It is argued here that the presence of large hydrostatic stresses at these boundaries provide nucleation sites for fracture of the debonding/decohesion type. Towards this end, a few 'proof of concept' types of experiments were designed to monitor the evolution of cracking during the tensile test. For the sake of monitoring the evolution of fracture, we concentrate on duplex alloys since they possess a little higher ductility. Thus, tensile specimens were mechanically polished and electropolished in the gauge section. The samples were strained isothermally at temperatures from RT to 500°C. The fracture evidence on the surface (normal to the loading direction) presumably indicates mixed mode fracture, i.e. combination of intergranular + transgranular, as shown in fig. 15 (*a*). However, the fracture evidence just below the fractured ends (parallel to the loading direction) indicate other minor fractures predominantly intergranular in origin (fig. 15 (*b*)) which appears to be in accord with the large stresses computed at the grain boundaries and triple points. Thus, it is argued that the presence of large hydrostatic stresses at these boundaries provide nucleation sites for fracture of debonding/ decohesion type. Once initiated, they propagate in a mixed mode, thereby masking the specific origin of the failure. Interestingly enough in all the specimens tested, the maximum failure strains were of the order of 2–4%, in good accord with the general ductility parameters presented by Kim (1992).

4.2. (Nearly lamellar) polycrystalline specimens with microstructural variations
4.2.1. Morphologically adding γ-phase in small quantities: 4% and 12% by volume
In the preceding section, it is demonstrated that grain boundaries are plausible sources of fracture initiation. Since the top 50% of the peak stress build-up is confined specifically to about 5 vol.% of the microstructure (estimated by the fraction of finite element meshes affected), close to the boundaries, it seems reasonable to attempt to alter these regions locally to affect the aggregate behaviour. The Ti–Al phase diagram in the vicinity of the Ti48–50 at.%Al composition provides the necessary means of incorporating some γ-TiAl at the grain boundaries. Duplex (D) and nearly lamellar (NL) microstructures are obtained by heat-treating the samples in the $\alpha + \gamma$ phase field. γ-TiAl formation occurs at grain boundaries and triple points (fig. 8 (*d*)), such that the grain is increasingly surrounded by a thin layer of γ depending on the holding time at temperature in the $\alpha + \gamma$ phase field. In the model this process is approximated by replacing tiny volumes (i.e., 4 and 12 vol.%) of lamellar material at the boundaries with γ (fig. 9 (*a*) and 9 (*b*)), and incorporating the deformation characteristics of the γ-TiAl phase. γ-TiAl single crystal data for Ti–56 at.%Al has $\tau_{crss} \approx 85$ MPa with strain hardening rate approximately 1500 MPa as obtained from Kawabata *et al.* (1985). Current literature suggests that γ-TiAl phase precipitated from Ti_3Al is softer (i.e., lower CRSS) due to lower interstitial contents in the transformed γ-TiAl phase. Thus values from Kawabata *et al.* (1985), are inflated estimates, and thus the simulations are rather conservative predictions of the beneficial effects of the actual γ response.

4.2.2. Flow response of the morphologically modified alloys
The theoretically simulated flow stress response is shown in fig. 16, along with the corresponding fully lamellar (material *A* with $g_1^0 = 50$ MPa, $g_2^0 = g_3^0 = 600$ MPa) stress–strain flow curve. Thus, substituting a small volume fraction of γ has a negligible effect on the flow stress. This output at first appears to be at odds with the experimental data. However, we recall that heat-treatment in the $\alpha + \gamma$ phase field to

incorporate γ-TiAl at the boundaries inhibits α grain growth, such that the grain size is scaled down. This has the net effect of raising the soft mode CRSS (as scaled through the Hall–Petch parameter) in the laminate morphology. Thus improvements in flow stress are primarily derived from grain size changes in the remaining α colony rather than due to any specific contribution of the γ phase itself. A rule of mixtures calculation shows that it is unreasonable to attribute the observed strengthening to the γ phase, especially since it demands strength parameters far in excess of those

Fig. 15
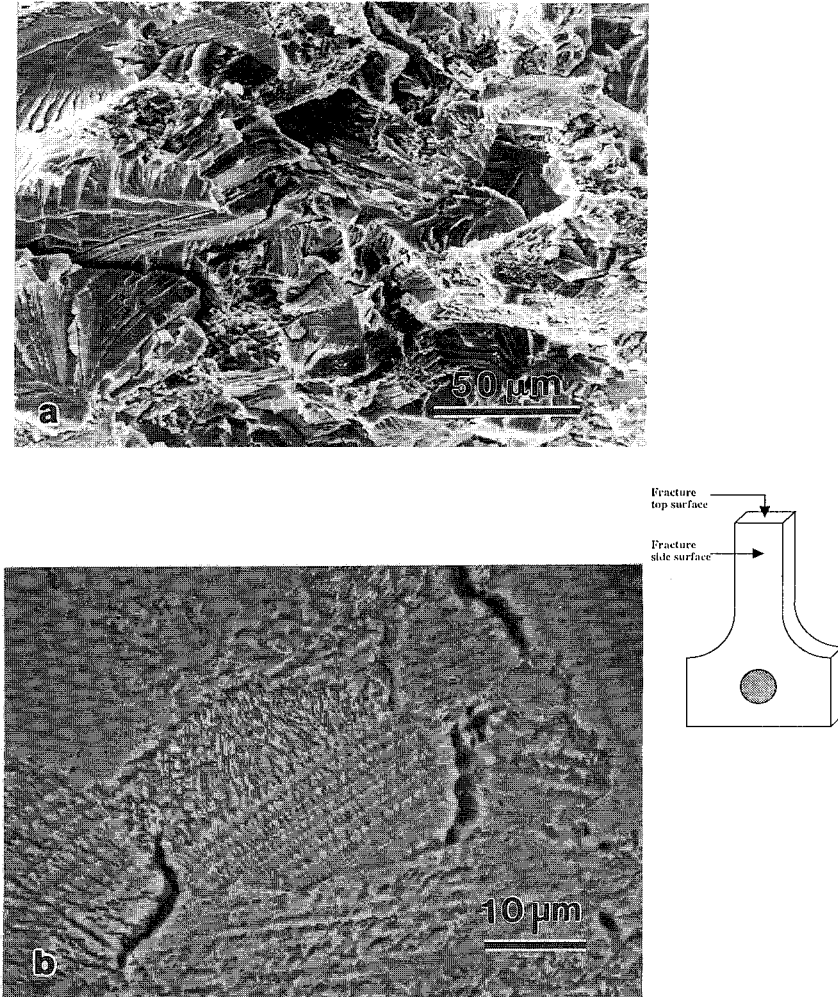
Scanning electron micrographs of the fracture evidence in Ti–Al, TiAl + *X* duplex alloy specimens deformed in tension from RT to 500°C. (*a*) Fracture evidence from the top (i.e., normal to the loading direction) of the fracture facet indicating, intergranular + transgranular mixed mode fracture, (*b*) fracture evidence from the side (i.e., parallel to the loading direction) of the sample gauge length just below the fractured edge. In this figure, the origin of the fractures appears to be predominantly intergranular.

Fig. 16
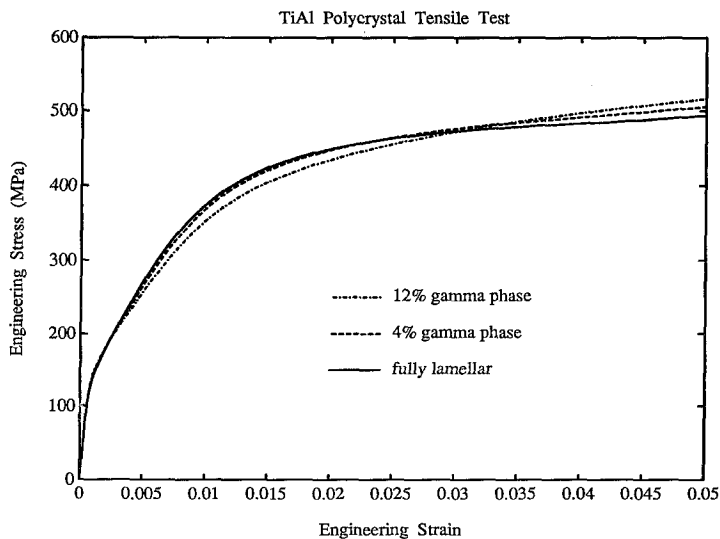
Stress–strain flow curve response in lamellar aggregate morphologically modified with 4, 8 and 12 vol.% γ-TiAl phase at the grain boundaries and triple points. Note that this intergranular phase has minimal effects on the flow stress.

measured in single crystals of TiAl. In our current simulations we have not altered the soft mode CRSS, as we are only substituting minuscule volume fractions of the γ phase. In instances where duplex structures are simulated, these effects will need to be incorporated. This remains an interesting avenue of exploration and will be reported in a later effort.

4.2.3. Hydrostatic stresses as related to fracture

Figure 17 shows the development of peak hydrostatic stresses (at 1% aggregate strain) in the modified simulation containing 12 vol.% γ-TiAl along with the base simulation of data sets for A (i.e., $g_1^0 = 50$ MPa, $g_2^0 = g_3^0 = 600$ MPa). While the general deformation features remain similar, the magnitude of peak hydrostatic stresses developed are significantly lower, which illustrates the 'effective' contribution of a softer more compliant γ-TiAl phase at specific sites of high stress concentrations. Figure 18 shows a plot of the peak hydrostatic stresses against macroscopic strain in samples with different volume fraction γ-TiAl compared to the base microstructure A. The peaks are monotonically lower for the NL microstructures. This decrease in the hydrostatic stress has a direct correspondence with the increase in strain to failure, see fig. 3 (*a*) and 3 (*b*). We contend that boundaries with high compatibility stresses are the nuclei of fracture initiation. Thus lowering the peak hydrostatic stress has the effect of statistically reducing the possible sites of failure initiation. This effect continues to improve up to the 12% volume fraction of γ-phase simulated till date.

The benefits accrued from the intergranular γ-TiAl phase remain marginal, on account of its high strain hardening rate ($= 1500$ MPa). The initial compliance of the γ-TiAl phase (because of low CRSS) is rapidly diminished as the flow-stress (in γ-TiAl) rises up to the lamellar hard mode yield stress. Nonetheless, this initial

Fig. 17

(a)

(b)
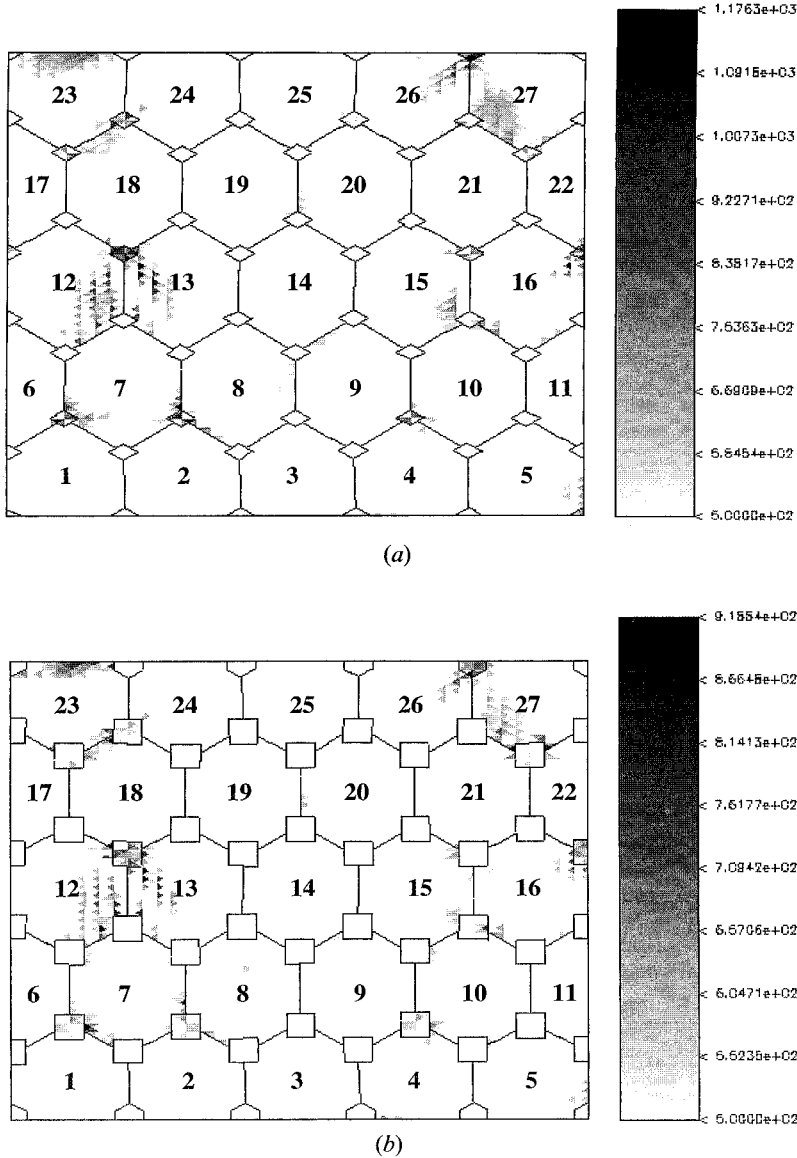
Contour of the hydrostatic stresses > 500 MPa, at 1% macroscopic strain, in the modified mesh containing (a) 4 vol.% and (b) 12 vol.% γ phase at triple points. The data set is generated for A with lamellar inputs as in A ($g_1^0 = 50$ MPa, $g_2^0 = g_3^0 = 600$ MPa) from fig. 16. Corresponding parameters for intergranular γ-TiAl phase are CRSS $= 85$ MPa, $\partial\tau/\partial\gamma = 1500$ MPa.

compliance is capable of accommodating incompatibilities across lamellar colonies, thereby reducing the incidence of fracture.

4.3. *Tension against compression effects*

While this paper, in large part, addresses tensile deformation, the essential features of strain localization and the subsequent peak hydrostatic stress distributions

Fig. 18
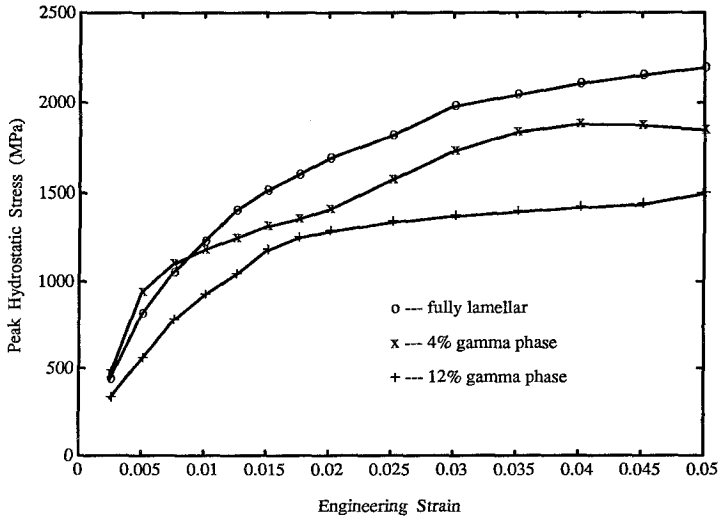
Composite plot of the peak hydrostatic stresses against macroscopic strain in samples with different volume fraction γ-TiAl (i) 4 vol.% and (ii) 12 vol.% compared to the base microstructure A ($g_1^0 = 50$ MPa, $g_2^0 = g_3^0 = 600$ MPa).

are expected to be similar in compression. For example, it was shown earlier that despite the uniaxial tensile environment (externally imposed) the actual stresses in the body range from tensile to compressive, see fig. 13 (*a*), 13 (*b*). Similar features of bipolar stresses are also observed in plain strain compression, fig. 19, though both the absolute value and the occurrence of peak hydrostatic stresses is significantly reduced. Scanning electron microscopy (SEM) studies (of the prepolished surfaces) of a FL specimen deformed approximately 3·5% in compression also reveals regions of mode I microcracking close to the boundaries, fig. 20, and are analogous to the tensile fracture observations presented earlier, see fig. 15. These results serve as a litmus test for the validity of the mathematical simulations. It is interesting to note that lamellar TiAl can sustain compressive strains on the order of 15–20% prior to failure. It is likely that additional features (crystal texturing effects, buckling of laminates, etc.) may evolve as deformation simulations are carried out to larger strains in compression. This is currently under study and details of lamellar TiAl under compressive loading will be reported elsewhere (Dao, Kad and Asaro 1994).

§5. SUMMARY AND CONCLUSIONS

The theoretical analysis and the experimental comparisons presented here provide a physical understanding of the underlying parameters responsible for the observed variations in mechanical properties, see fig. 3 (*a*), 3 (*b*), between fully lamellar (FL) and nearly lamellar (NL) microstructures. The identification of possible fracture initiation sites at the grain boundary (triple points in particular), on account of the large hydrostatic stresses, helps elucidate specific factors responsible for the microstructural dependent ductile behaviour. Thus, while experimental stress–strain plots are a mere measure of the gross plastic response, the hydrostatic stress–strain plots, see fig. 18, reflect a more detailed microstructural sensitivity to plastic deformation. In

Fig. 19
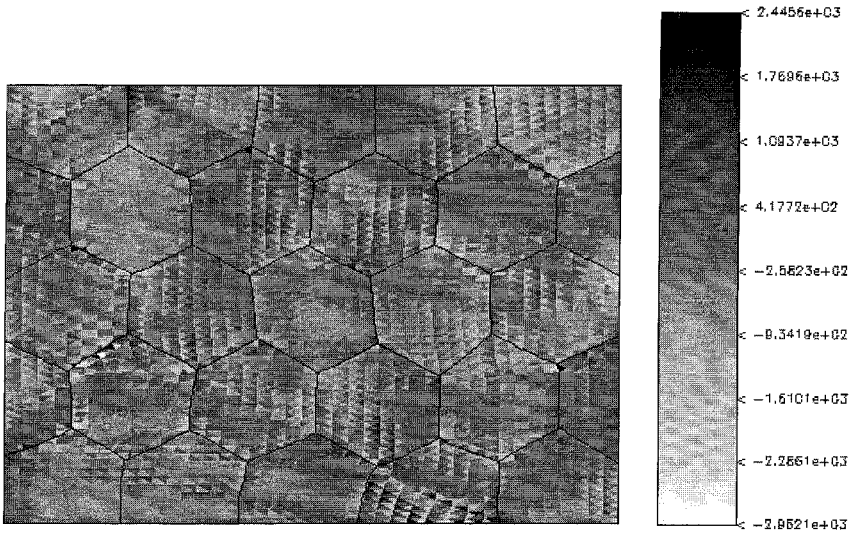
Contour plot of the development of hydrostatic stresses in the deformed mesh at 5% macroscopic compressive strain. Note the strong tensile hydrostatic components, that may be responsible for cracking in compression. The data sets is generated for A ($g_1^0 = 50$ MPa, $g_2^0 = g_3^0 = 600$ MPa).

Fig. 20
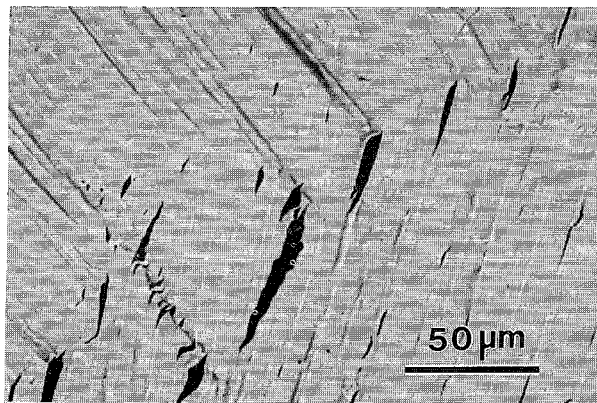
Scanning electron micrographs of the fracture evidence in fully lamellar (FL) sample deformed $\approx 3 \cdot 5\%$ in compression at RT. The fracture evidence gathered from the side (i.e., parallel to the loading direction) of the pre-polished sample.

essence, the peak hydrostatic stress is analogous to a 'fracture stress' in that it provides some measure of the stress prior to complete failure. Within that context, for a given 'fracture stress', the theoretically computed results of fig. 18 accurately predict the general features of experimental observations (schematically illustrated in fig. 3 (*b*)) of increasing strain to failure as the ratio of γ-grain to lamellar-grain increases. In this present effort, for reasons of space, and in order to permit a detailed presentation of the methodology, only pertinent mechanical and microstructural variations have been presented. Systematic studies of other periodic and non-periodic microstructural variations, with different deformation histories can be performed similarly, within the framework detailed here, and will be reported in subsequent efforts. The general experimental features presented in §4, the development of hydrostatic stresses, are explained as follows.

5.1. *Localized deformations*

The natural tendency of non-uniform deformations has been clearly illustrated in the preceding section on strain accumulations (§4.1.2) and lattice rotations (§4.1.3). Since these characteristics arise in the continuum two-dimensional polycrystal model, it appears then that they are due mostly to the gross characteristics of crystallographic slip, along with the heterogeneity in the material properties (i.e. grain interactions). Note that, excluding the effect of the boundary conditions at the edges of the two-dimensional model microstructure, some of the most active strain accumulations and lattice rotations occur in the vicinity of the grain boundaries. Thus, strain incompatibilities across slip discontinuities such as grain boundaries create constraints (described in §5.2) between adjacent crystals. In particular, the most active region is the 12–13–18 triple point, figs. 11 and 12, suggesting that they may even act as initiators of non-uniform (or perhaps even localized) deformation modes. In fact, similar features are also expected to develop in nominally ductile materials like aluminium and copper (Harren *et al.* 1988). However, with 12 identical slip systems (and five independent slip systems satisfying the Von Mises criteria of macroscopic plasticity), these effects are mitigated for aluminium and copper polycrystalline aggregates at low strains. Similarly, incompatibilities arising out of specific misorientations between adjacent crystals are also muted on account of the 12 slip systems available. Needless to say that these effects will be exacerbated in the event of (i) limited availability of slip systems, and (ii) non-equivalence or a large CRSS anisotropy for the individual slip systems. Both problems (i) and (ii) exist in two phase γ-TiAl + α_2-Ti$_3$Al lamellar microstructures (Kad *et al.* 1993), and strain incompatibilities (and consequently, the development of large stresses) across neighbouring crystals are a natural outcome of such limitations.

5.2. *Constraint effects*

Deformation incompatibilities in elastic–plastic phase aggregates (i.e., α_2 and γ are the idealized elastic and plastic phases, respectively) can be manifested both microscopically and macroscopically. Microscopic effects play a role at the onset of plastic deformation since, geometrically necessary dislocations must be generated to accommodate the lack of deformation in the elastic phase. The elastic phase (in an elastic–plastic phase aggregate) provides additional constraints that effectively increase the yield strength of the plastic phase. This constraint is manifested on a macroscopic

Fig. 21

(*a*)   (*b*)
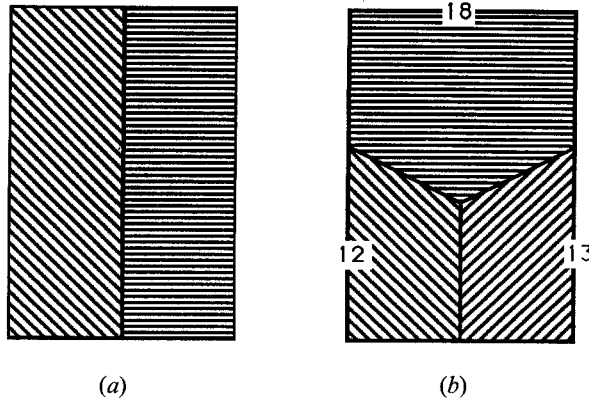
(*a*) Lamellar bicrystal with orientations $\psi = 0°$ and 45° in the individual colonies. The hard orientations exhibits a strong constraint on the soft crystal and the bicrystal is strengthened beyond the volume average yield stress. (*b*) Extension of the bicrystal constraint to the polycrystalline grid of fig. 8. The triple point constraint between crystals 12, 13 as constrained by crystal 18 is illustrated.

level (Saxton, West and Barrett 1971) and depends only on the elastic phase volume fraction and not on its scale.

The strengthening effects of hard phases in two-phase aggregates are well known and are often represented by the volume fraction weighted composite equation. For continuous reinforcements of α_2 phase in lamellar TiAl, with an epitaxial relationship, the α_2 reinforcements play a decidedly larger role in dictating material response than possible by their volume fraction alone in the above mentioned composite equation. Two examples of constraint based strengthening are; (i) positive deviation of yield stress from the mixture rule as observed on increasing α_2 phase volume fraction (Umakoshi and Nakano 1993), and (ii) the observation of large Hall–Petch slope in polycrystalline aggregates (Kim 1993) of lamellar material over their single crystal counterparts (Umakoshi and Nakano 1993).

For hard mode deformation in lamellar TiAl-based alloys, Lee, Ahzi, Kad and Asaro (1993) suggest that the high CRSS values for pyramidal slip in α_2 phase impose kinematic constraints on the softer γ-phase. In the current context, we pursue similar constraints between adjacent crystals with different orientations (and hence with different yield and flow behaviour) such that the soft orientations ($\psi = 45°$) are constrained by the hard orientations ($\psi = 0°$, 90°), provided the integrity of the interface (grain boundary in this case) is preserved. Figure 21 (*a*) shows a bicrystal schematic with individual orientations $\psi = 0°$ (crystal 1) and 45° (crystal 2) with a CRSS of 50 MPa (soft mode) and 600 MPa (hard mode), respectively. Thus, boundary constraints prevent the soft mode from operating freely, beyond some initial deformation, as further slip in crystal 1 requires propagation through the α_2 harder phase in crystal 2. Initial calculations and experimental observations indicate that relatively small misorientations ($\approx 15°$) are sufficient to generate large incompatibilities at grain boundaries that invariably lead to cracking, or debonding of the α_2/γ interfaces in the proximity of the interface, fig. 20. The bicrystal example is extended to the random polycrystalline grid, see fig. 8 (*a*), used in the current calculations. The

triple point region between crystals 12, 13 and 18 (with peak hydrostatic stresses) is enlarged in fig. 21 (*b*). Here the near soft mode orientation in crystals 12 and 13 is constrained by the hard mode orientation in crystal 18. Thus, the beneficial effects of the soft orientation are rapidly lost in the presence of an adjacent hard orientation constraint. More importantly, strain incompatibilities result in large hydrostatic stresses, the magnitude of which is dominated by the hard mode CRSS ($=600$ MPa) and hard mode hardening ($=1500$ MPa) parameters.

5.3. *Orientation dependent strengthening*

The anisotropic flow properties in single crystals (or colonies) of lamellar TiAl are particularly dependent on the lamellar normal orientation with respect to the loading axis (Yamaguchi and Umakoshi 1990). Thus the soft orientation (at 45° with respect to the loading axis) is derived by confining the deformation, largely inhomogeneously to the soft γ phase, parallel to the direction of maximum shear. Deformation band formation is a natural consequence of such localized activity, especially at large strains. Similar inhomogeneous strain accumulations are encountered in simulations for polycrystalline aggregates, see fig. 11 (*a*) and 11 (*b*). For uniaxial tension/ compression deformation in single crystals, rotations of the lamella about the loading axis are irrelevant such that orientations ψ and $\psi \pm 90°$ are equivalent, see fig. 6 (*b*) and fig. 8. However, in polycrystalline aggregates, the direction of maximum shear spans several crystals of random orientations. Since macroscopic plasticity dictates that the deformation band traverse the entire cross-section, one can imagine additional constraints arising from the specific orientation of the individual crystal with respect ot the macroscopic deformation band as shown in fig. 22. The non-

Fig. 22

(*a*)   (*b*)
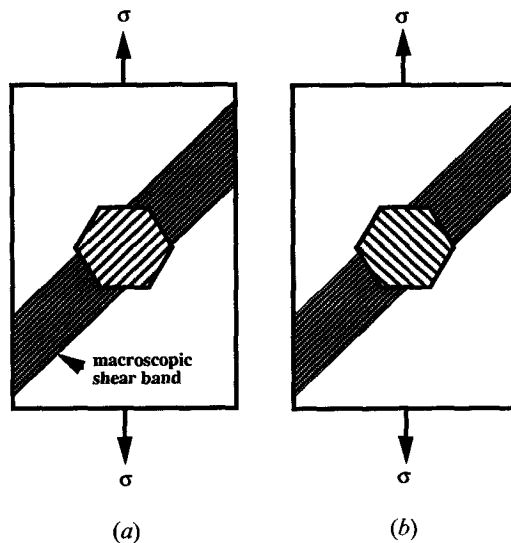
Schematic of the non-equivalence of the $\psi = 45°$ and $\psi = 45° \pm 90°$ crystal orientations in the polycrystalline mesh in fig. 8. The resistance to the propagation of a macroscopic deformation band is ascertained by whether the band is (*a*) parallel or (*b*) perpendicular to the laminates.

equivalence of ψ and $\psi \pm 90°$ orientations in polycrystalline aggregates is evident, fig. 22. Note that the location of a deformation band in polycrystals is dictated by aggregate properties (for example: the orientation of neighbouring crystals, texture within the deformation band, etc.) rather than a single orientation. Thus, the mere incidence of a soft orientation does not guarantee a lower flow stress as strain anisotropies parallel or perpendicular to the laminate will require a low and a high stress, respectively. Perhaps the best example to illustrate such orientation effects is the small deformation (or shear) band (going lower-left to upper-right corner) traversing through crystals 6, 7, 12, 13, 19, 20, and 26 at 5% macroscopic strain, see fig. 11 (*b*). This deformation band is approximately parallel and perpendicular to the lamellae in crystals 19 and 26, respectively. The strain accumulations are similar in crystals 19 and 26 (fig. 11 (*b*)), but the hydrostatic stresses are significantly higher in crystal 26 on account of deformation incurred perpendicularly. Note that the strain anisotropy is approximately parallel to the lamellae in crystal 20, and could possibly be accomplished by delamination of either γ–γ plates, or γ–α_2 plates and slip parallel to the laminates in the soft γ phase. These features will be addressed in detail in subsequent articles.

5.4. *Deformability of γ-TiAl in duplex microstructures*

The identification of possible fracture initiation sites at the grain boundary (triple points in particular), on account of the large hydrostatic stresses, helps formulate the specifics of the problem at hand. This is a constructive step towards microstructural design in that it pinpoints the beneficial effect of an increasing γ-TiAl volume fraction. Thus, the build-up of large hydrostatic stresses is altered by varying the microstructural mix of lamellar and γ morphologies. Certainly the improvements in ductile behaviour are tied in with the more compliant flow properties in the regions close to the grain boundaries. In this regard, deformation characteristics of the γ phase deserve special attention. Thus, factors controlling the compositional variations (Hall and Huang 1989), the mobility of dislocations (Court, Vasudevan and Fraser 1990) and interstitial impurity concerns (Kad and Fraser 1994) are important in that they affect the flow behaviour (i.e., CRSS and strain hardening). The specific values for the single phase TiAl at the boundaries, (CRSS ≈ 85 MPa with $\partial\tau/\partial\gamma \approx 1500$ MPa for the single phase TiAl (Kawabata, Kanai and Izumi 1985)) were originally obtained from alloys of Ti–56 at.%Al composition with a somewhat higher interstitial impurity. In contrast, in Ti–48 at.%Al alloys, γ has a composition of about 50 at.%Al and has a much lower interstitial content on account of the gettering effects of the α_2 phase (Vasudevan, Stucke, Court and Fraser 1989). Thus values from Kawabata *et al.* (1985), are inflated estimates such that the theoretical computations provide a rather conservative prediction of the beneficial effects of the γ phase response in the NL microstructures. The benefits accrued from the intergranular γ-TiAl phase remain marginal, on account of its high work-hardening parameters, $\partial\tau/\partial\gamma = 1500$ MPa. At the onset of plastic deformation, the low CRSS of the γ-TiAl phase at the boundaries, presents an alternative to the hard mode CRSS encountered in the adjacent crystal. However, this initial compliance is rapidly diminished as the flow stress (in γ-TiAl) rises up to the lamellar hard mode yield stress. Since $\partial\tau/\partial\gamma$ (hard mode) $= \partial\tau/\partial\gamma(\gamma\text{-TiAl}) = 1500$ MPa, no further benefits are derived. Assuming linear hardening, as employed throughout in the numerical calculations presented here, the maximum allowable local shear strain in γ-TiAl is about 35%, adjacent to a crystal in ideal hard mode orientation (i.e. $\psi = 0°$ or 180°). Looking back at the strain

accumulation of fig. 11 (*a*), 11 (*b*), we note that maximum shear strain is about 14% and 58% for 1% and 5% aggregate strain, respectively. Thus the maximum beneficial effect of γ, is clearly exhausted at strains less than 5% aggregate strain; in concert with experimental fracture strains typically within the 2–4% region. Nonetheless, the initial compliance is, capable of accommodating incompatibilities across lamellar colonies, thereby reducing the incidence of fracture. It is noted that inserting small volume fractions of γ-TiAl is perhaps a simplified approach to a complex problem. Realistically, a similar situation may be derived by the coarsening of the laminates close to the grain boundaries, see fig. 9 (*c*). This has a net effect of increasing lamellar spacing, adjacent to the boundaries, which in turn lowers the applicable input value for hard mode τ_{crss}^{hard}. Such finer modifications will be dealt with later. To the best of our knowledge, such an understanding, and more specifically such an approach to materials modelling in lamellar TiAl alloys is currently not available.

REFERENCES

ASARO, R. J., 1979, *Acta metall.*, **27**, 445.
ASARO, R. J., and RICE, J. R., 1977, *J. Mech. Phys. Solids*, **25**, 309.
BISHOP, J. F. W., 1954, *J. Mech. Phys. Solids*, **3**, 130.
CHAN, K. S., and KIM, Y.-W., 1991, *Microstructure/Property Relationships in Titanium Aluminides and Alloys*, edited by Y.-W. Kim and R. R. Boyer (Warrendale, PA: TMS), p. 179; 1992, *Metall. Trans.*, (to be published).
COURT, S. A., VASUDEVAN, V. K., and FRASER, H. L., 1990, *Phil. Mag. A*, **61**, 141.
DAO, M., and ASARO, R. J., 1993, *Mater. Sci. Engng A*, **170**, 143.
DAO, M., KAD, B. K., and ASARO, R. J., 1994, *MRS Symp. Proc.*, **322**, in press.
DAVIDSON, D. L., and CAMPBELL, J. B., 1993, *Metall. Trans. A*, **24**, 1555.
DÈVE, H., HARREN, S. V., MCCULLOUGH, C., and ASARO, R. J., 1988, *Acta metall.*, **36**, 341.
DILLAMORE, I. L., and KATOH, H., 1974, *J. metal Sci.*, **13**, 73.
FUJIWARA, T., NAKAMURA, A. M., HOSOMI, M., NISHITANI, S. R., SHIRAI, Y., and YAMAGUCHI, M., 1990, *Phil. Mag. A*, **61**, 591.
HALL, E. L., and HUANG, S. C., 1989, *J. mater. Research*, **4**, 595.
HARREN, S. V., and ASARO, R. J., 1989, *J. Mech. Phys. Solids*, **37**, 191.
HARREN, S. V., DÈVE, H. E., and ASARO, R. J., 1988, *Acta metall.*, **36**, 2435.
HILL, R., and RICE, J. R., 1972, *J. Mech. Phys. Solids*, **20**, 401.
INUI, H., OH, M. H., NAKAMURA, A., and YAMAGUCHI, M., 1992, *Acta metall.*, **40**, 3095.
KAD, B. K., and FRASER, H. L., 1994, *Phil. Mag. Lett.*, **70**, 211.
KAD, B. K., HAZZLEDINE, P. M., and FRASER, H. L., 1993, *MRS Symp. Proc.*, 288, 495.
KAWABATA, T., KANAI, T., and IZUMI, O., 1985, *Acta metall.*, **33**, 1355.
KIM, Y.-W., 1989, *J. Metals*, **41**, 24; 1992, *Acta metall.*, **40**, 1121.
LEE, B. J., AHZI, S., KAD, B. K., and ASARO, R. J., 1993, *Scripta metall.*, **29**, 823.
LIPSITT, H. A., SCHECHTMAN, D., and SCHAFRIK, R. E., 1975, *Metall. Trans. A*, **6**, 1991.
MCHUGH, P. E., ASARO, R. J., and SHIH, C. F., 1993, *Acta metall.*, **41**, 1461.
MENDIRATTA, M. G., KIM, Y.-W., and DIMIDUK, D. M., 1993, *MRS Symp. Proc.*, 288, 543.
NAKANO, T., YOKOYAMA, A., and UMAKOSHI, Y., 1992, *Scripta metall.*, **27**, 1253.

PIERCE, D., ASARO, R. J., and NEEDLEMAN, A., 1982, *Acta metall.*, **30,** 1087; 1983, *Ibid.*, **31,** 1951.

SAXTON, H. J., WEST, A. J., and BARRETT, C. R., 1971, *Metall. Trans.* A, **2,** 999.

TAYLOR, G. I., 1938 *a*, *J. Inst. Metals*, **62,** 307; 1938 *b*, *Stephen Timoshenko 60th Anniversary Volume*, edited by J. M. Lessels (New York: Macmillan), p. 218.

UMAKOSHI, Y., NAKANO, T., and YAMANE, T., 1991, *Scripta metall.*, **25,** 1525.

VASUDEVAN, V. K., STUCKE, M. A., COURT, S. A., and FRASER, H. L., 1989, *Phil. Mag Lett.*, **59,** 299.

YAMAGUCHI, M., and UMAKOSHI, Y., 1990, *Prog. mater. Sci.*, **34,** 1.